Experimental Measurements of the Power Output of a Cu/Cu^{2+} Thermogalvanic Brick

by

William Lee

A Thesis Presented in Partial Fulfillment
of the Requirements for the Degree
Master of Science

Approved November 2018 by the
Graduate Supervisory Committee:

Patrick Phelan, Chair
Mounir El Asmar
Ryan Milcarek

ARIZONA STATE UNIVERSITY

December 2018

ABSTRACT

Buildings continue to take up a significant portion of the global energy consumption, meaning there are significant research opportunities in reducing the energy consumption of the building sector. One widely studied area is waste heat recovery. The purpose of this research is to test a prototype thermogalvanic cell in the form factor of a UK metric brick sized at $215\,mm \times 102.5\,mm \times 65\,mm$ for the experimental power output using a copper/copper(II) (Cu/Cu^{2+}) based aqueous electrode. In this study the thermogalvanic brick uses a 0.7 M $CuSO_4$ + 0.1 M H_2SO_4 aqueous electrolyte with copper electrodes as two of the walls. The other walls of the thermogalvanic brick are made of $5.588\,mm$ ($0.22\,in$) thick acrylic sheet. Internal to the brick, a 0.2 volume fraction minimal surface Schwartz diamond (Schwartz D) structure made of ABS, Polycarbonate-ABS (PCABS), and Polycarbonate-Carbon Fiber (PCCF) was tested to see the effects on the power output of the thermogalvanic brick. By changing the size of the thermogalvanic cell into that of a brick will allow this thermogalvanic cell to become the literal building blocks of green buildings. The thermogalvanic brick was tested by applying a constant power to the strip heater attached to the hot side of the brick, resulting in various ΔT values between 8°C and 15°C depending on the material of Schwartz D inside. From this, it was found that a single Cu/Cu^{2+} thermogalvanic brick containing the PCCF or PCABS Schwartz D performed equivalently well at a 163.8% or 164.9%, respectively, higher normalized power density output than the control brick containing only electrolyte solution.

ACKNOWLEDGMENTS

I would like to give a big thank you to Dr. Phelan, Dr. El Asmar, and Dr. Milcarek for being part of my supervisory committee. I would especially like to thank Dr. Phelan for his guidance and for providing the opportunity to work on this project.

Special thanks to Andrey Gunawan and Nicholas Fette for the assistance and consulting throughout this project. Another special thanks to the project collaborators, Dr. Leigh Aldous from Kings College and Dr. Robert Taylor from UNSW for their contributions to this project.

I would also like to acknowledge my peers Benjamin Obeng and Ryan Kiracofe for their hard work on this project; it has been quite interesting and enlightening experience working along side these people.

Finally, I am grateful to Intel for sponsoring my degree, as well as my manager, Rakesh Ramachandran, for supporting me through this program.

TABLE OF CONTENTS

CHAPTER Page

LIST OF TABLES

LIST OF FIGURES

Figure Page

Figure Page

Figure Page

Figure Page

Figure Page

Chapter 1

INTRODUCTION

As of 2017, global energy consumption has reached the equivalent of 13,511 million tonnes of oil a year, which is up by 2.2% per annum from 2016 [1]. Not only has the worldwide energy consumption grown rapidly in the past decade, but also the global carbon dioxide emissions growth rate per annum is up to 1.6% with a total of 33,444 million tonnes of carbon dioxide emitted in 2017 [1]. Following the current trends, this energy consumption number is projected to continue to grow as humans continue to populate the earth and develop new societies and technologies.

Recent concerns with the rising energy consumption and carbon dioxide emission of humans has acted as a catalyst for research into alternate ways of harnessing energy; over the past 11 years, the renewable energy usage has more than quadrupled, growing at a rate of 17% per annum [1–3]. And to take a look into the future, in a report by the International Energy Agency, the use of renewable energy sources is predicted to reach a value of 12.4% of the total energy use by 2023 [4]. One such area of renewable energy is electrochemical cells; electrochemical cells, more commonly referred to as voltaic cells or galvanic cells, are one of the ways which chemical energy is stored and converted into electricity. The consumer batteries that are ubiquitous in today's society are composed of multiple electrochemical cells wired in parallel or in series.

The roots of electrochemical cells date back to a 1791 report written by Luigi Galvani on animal electricity [5]. Galvani noted in his observations of dissected frogs, muscle contractions when nerves were connected using different metal plates, seen in Figure 1.1 [5, 6]. Galvani concluded from his experiments that animals contain some sort of inherent electricity that manifests within muscles and nerves [5, 7].

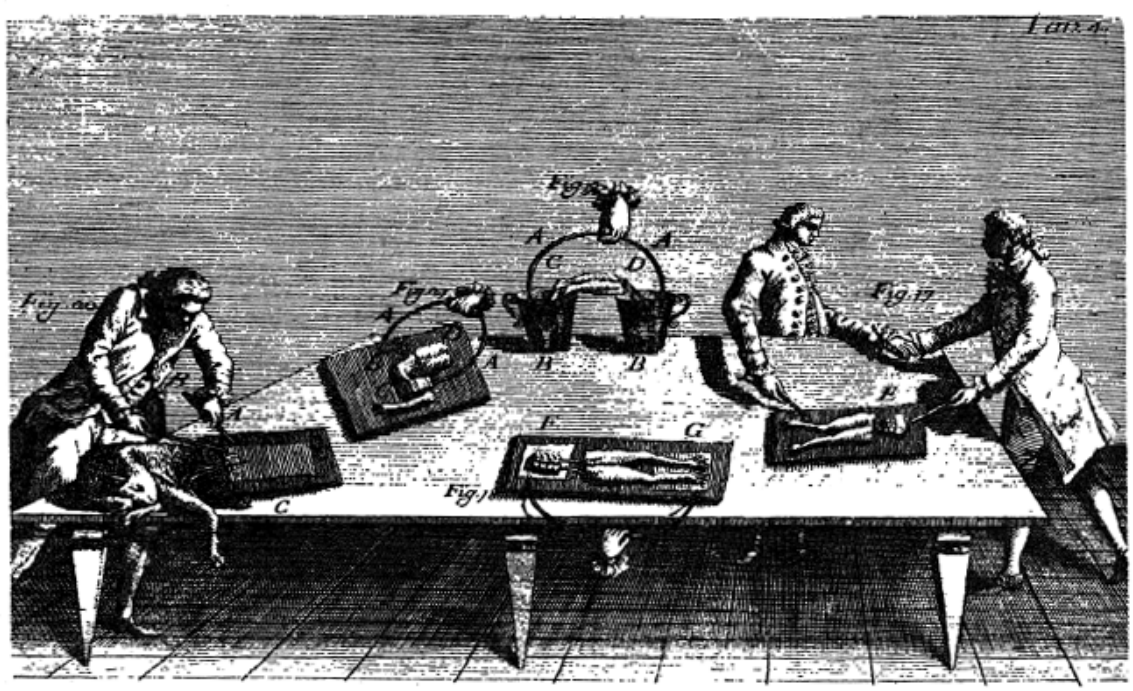

Figure 1.1: Depiction of Various Experiments Performed by Luigi Galvani on Animal Electricity [5].

Galvani's findings marked the beginning of rapid advancements in electrochemistry, leading to the creation of the voltaic pile. Alessandro Volta, a physicist, disagreed with Galvani's claims concerning animal electricity; Volta then created a device to prove the dead frog only reacted to an electrical stimuli caused by the dissimilar metals [6, 7]. Using alternating metal plates with wires connected to the opposing ends, Volta created what is now known as the voltaic pile which generated a spark when the opposing wires were brought together [6, 7].

The particular type of electrochemical cell evaluated in this paper is a thermogalvanic cell. In its simplest form, a thermogalvanic cell is an electrochemical cell that converts thermal energy into electricity. The temperature difference between two metallic electrodes drives a chemical reaction to take place, which generates a

potential that is proportional to the entropy flux [8, 9]. The ability to convert heat into electricity has the potential to become an extremely valuable asset to humanity as there are many untapped sources of heat and waste heat around us today. Industrial applications are particularly notorious for the amount of waste heat and green house gases generated; the heat energy that is left unused and dumped into the environment becomes wasted energy in amounts difficult to quantify [10–12]. Motorized transportation is another generator of large amounts of waste heat and carbon emissions, because as much as 80% of fuel may be lost as waste heat [13–15]. The building and data center sector should also not be left out of the equation for waste heat generation, as buildings worldwide consume over a third of global yearly energy usage and about two thirds of that generated energy is lost as waste heat [16–19].

In the area of thermogalvanics, the research scene has been expanding rapidly over the past 8 years, which can be noted by the number of publications on the topic of thermogalvanic cells in Figure 1.2. Particular interest in low grade heat source driven thermogalvanic cells utilizing various electrolyte material can be seen through both old and new studies [8, 9, 20–33]. A recent study of low-grade heat energy (under 100°C) electrochemical system has found a relatively high—for thermogalvanic standards—thermal to electrical energy conversion efficiency of 5.7% [26].

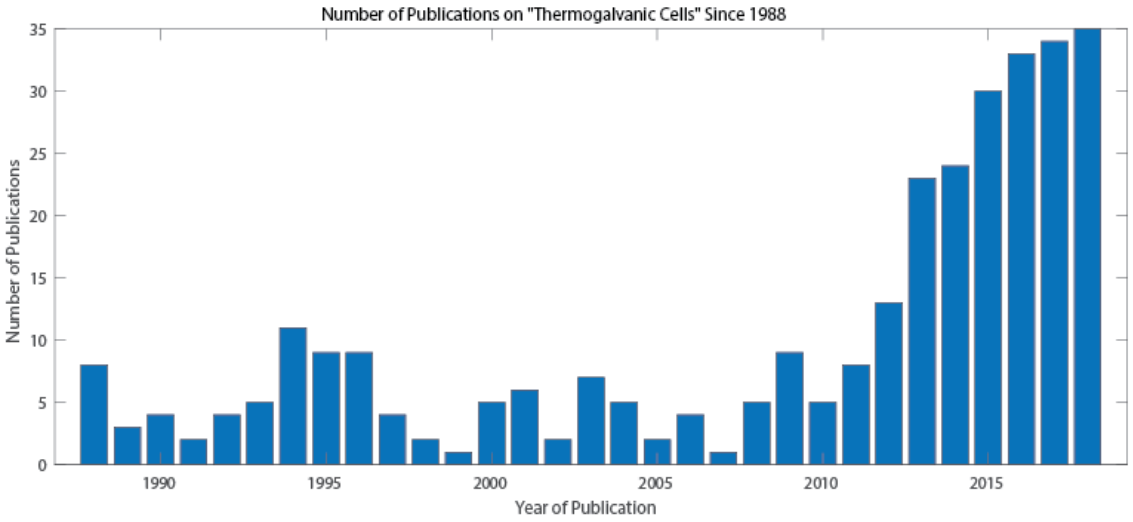

Figure 1.2: A Bar Plot Showing Data for the Number of Publications on the Topic of Thermogalvanic Cells from Dimensions [34].

1.1 Motivation

Globally, a large portion of the energy consumed is used to regulate the thermal requirements (cooling and heating) of industrial and residential buildings and a significant chunk of that energy consumed is lost as waste heat [10, 11, 16, 35]. The idea behind this project is to scale a thermogalvanic cell to the size of a standard UK metric brick at $215\,mm \times 102.5\,mm \times 65\,mm$ where it can become the literal building blocks for future energy efficient buildings. Built into the walls of a building, the thermogalvanic brick will utilize the temperature gradient between the external environment and the internal building temperature to drive the reduction-oxidation (redox) reaction and generate electricity.

To put this into perspective, 22% of new single family homes built in 2017 in the United States used brick as the building material [36]. With an average size of $2,426\,ft^2$ (or $225.3828\,m^2$), assuming only single story houses, each of these homes ($8\,ft$ ground to ceiling) would use, on average, $8,786$ UK metric sized bricks for the

external walls [36]. Replacing some or potentially all of the over $8,700$ bricks in the exterior walls of a home with thermogalvanic cells would allow the homeowner to recover some of the energy used to regulate the thermal requirements of their home.

1.2 Project Goals

The overarching goal of this project is to design, prototype, test, and develop a thermogalvanic cell in the form of a brick that can serve as a low-cost way to recover some of the used energy for thermal regulation in buildings while also meeting or exceeding the ASTM standard for structural stability of a standard brick.

1.2.1 Project Specific Goals

The scope of the overarching project goal is quite a large task for a single person to complete in a timely fashion. Hence, the project has been split into various subsections for examination and research while maintaining the end goal of a commercially available brick. The main area of interest of the thermogalvanic brick examined in this paper is the experimental power output of a horizontally orientated thermogalvanic brick using the copper/copper(II) (Cu/Cu^{2+}) reduction-oxidation reaction. The second area of interest is how adding a 3D printed 0.2 volume fraction minimal surface Schwartz diamond (Schwartz D) structure—seen below in Figure 1.3 for the 3D model and Figure 1.4 for the printed structures—changes the power output.

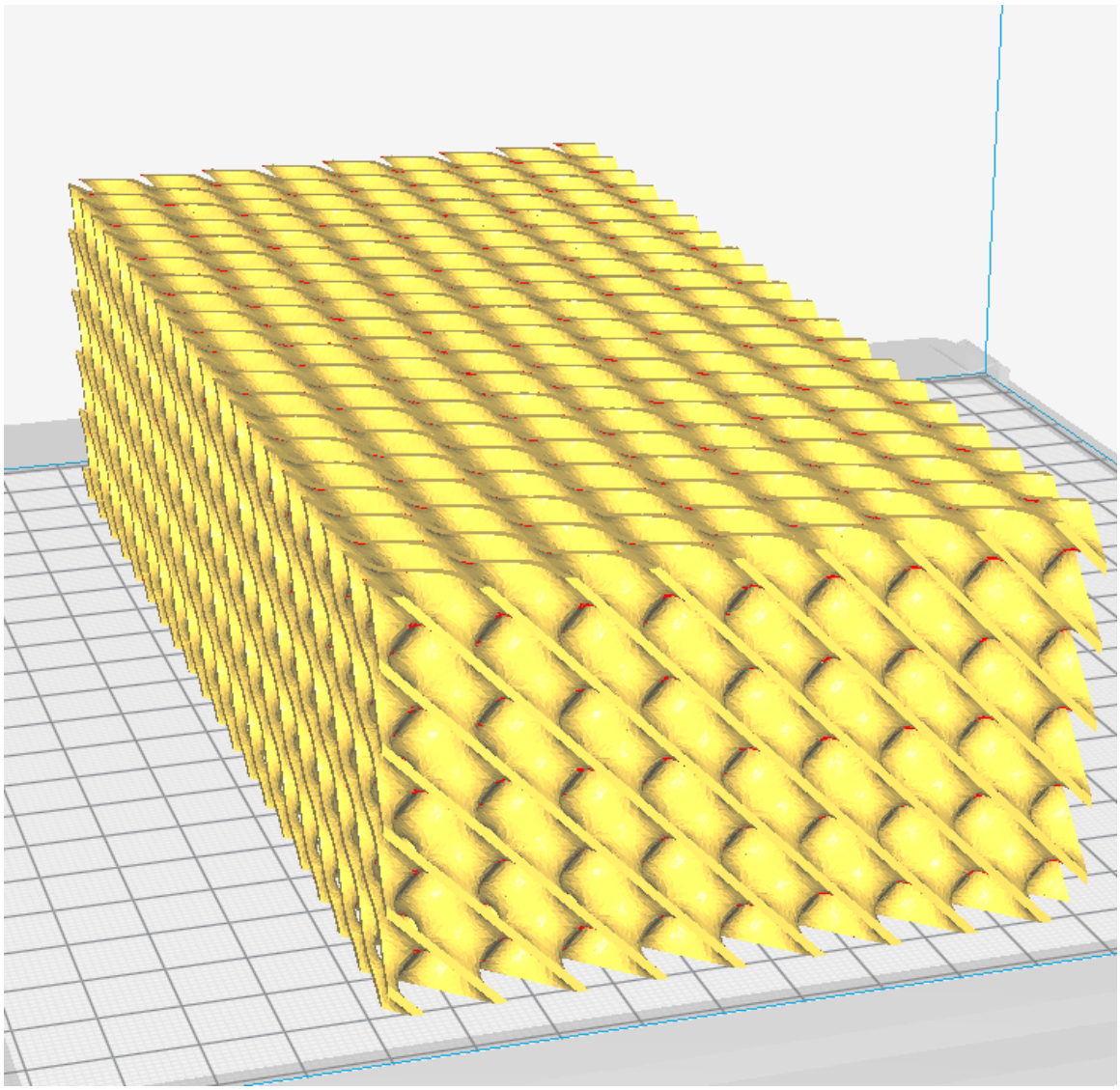

Figure 1.3: A 3D Model of the Schwartz D Structure to be Used in the Thermogalvanic Brick.

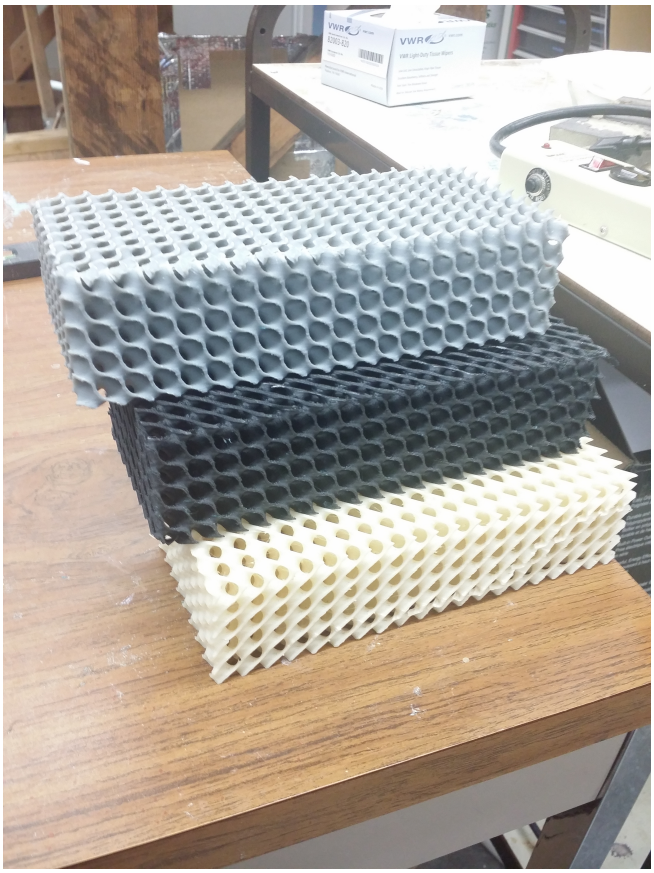

Figure 1.4: A Physical 3D Printed Model of the Schwartz D Structures Used in the Thermogalvanic Brick From Top to Bottom, Acrylonitrile Butadiene Styrene (ABS), Polycarbonate Carbon Fiber (PCCF), Polycarbonate Acrylonitrile Butadiene Styrene (PCABS).

1.3 Theory

The thermogalvanic brick is a combination of mechanical, thermal, chemical, and electrical interactions in a single system. One of the main points of interest in a thermogalvanic cell is the maximum power output (P_{max}) that the cell can generate, which will be the focus of this paper. The other key component of a thermogalvanic cell would be the Seebeck coefficient which has been previously studied for the specific

0.7 M $CuSO_4$ + 0.1 M H_2SO_4 aqueous electrolyte chosen in this paper [9, 28].

1.3.1 Reduction-Oxidation of Copper/Copper(II) in an Aqueous Electrolyte

An aqueous copper (II) sulfate ($CuSO_4$) electrolyte solution undergoes a redox reaction when subject to a temperature gradient across two copper electrodes as seen in Figure 1.5.

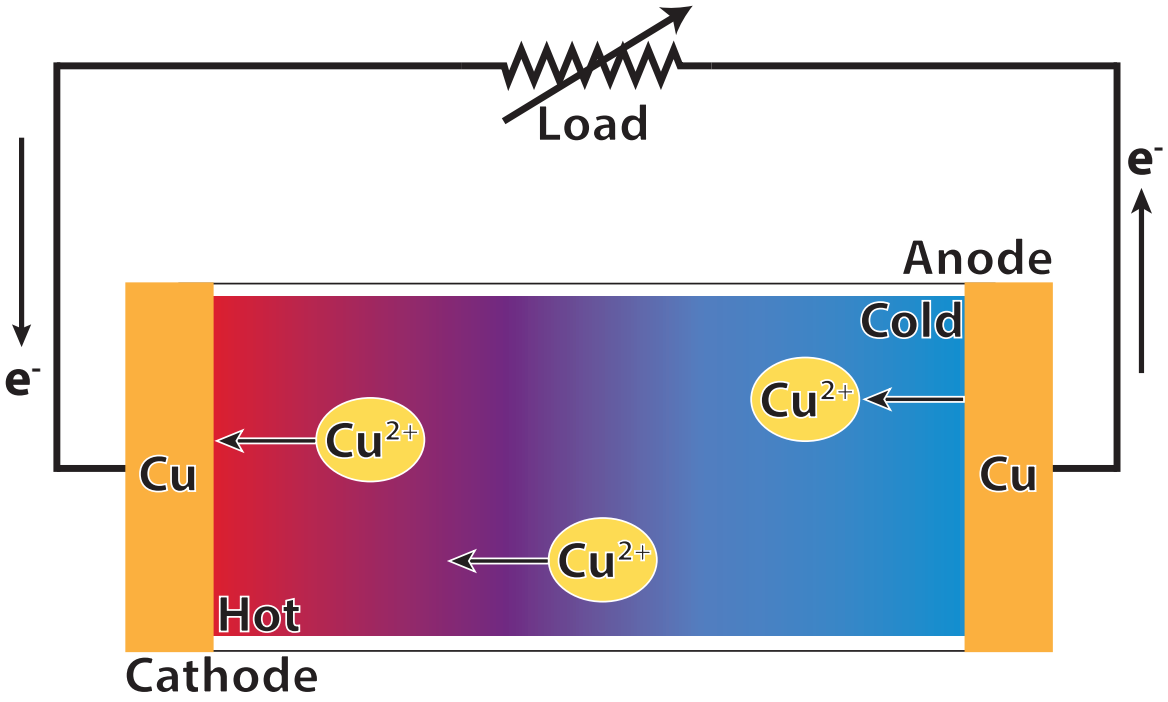

Figure 1.5: A Depiction of the Cross Section of an Aqueous $CuSO_4$ Electrolyte Thermogalvanic Brick with Copper Electrodes.

Starting with the anode, the oxidation of copper occurs when a load is applied across the electrodes due to the potential difference between the electrodes caused by the temperature difference across the cell [8, 9, 28]. The oxidation reaction can be described as:

$$Cu \longrightarrow Cu^{2+} + 2\,e^{-} \tag{1.1}$$

while the reduction at the cathode is described below:

$$\mathrm{Cu}^{2+} + 2\,\mathrm{e}^{-} \longrightarrow \mathrm{Cu} \tag{1.2}$$

Through two half-reaction pairs of the redox reaction described above, the thermal energy is thus converted into electricity. This is because of the potential difference in the copper electrodes to the aqueous copper(II) which is known as the standard electrode potential. Hence, the energy output of the copper/copper(II) redox reaction seen in equations 1.1 and 1.2 can be quantified with a standard electrode potential of $0.339\,V$ [37].

1.3.2 Maximum Power Output

The maximum power output is determined from the current output of the thermogalvanic brick. From Ohm's Law it is known that:

$$V = IR \tag{1.3}$$

and for power:

$$P = IV \tag{1.4}$$

where V is the voltage, I is the current, R is the resistance, and P is the power in a circuit. Applying Ohm's Law to the thermogalvanic brick, it can be found that:

$$E = IR_{ext} \tag{1.5}$$

where E is the cell potential (equivalent to V in equations 1.3 and 1.4), I is the current, and R_{ext} is the external resistance applied in series to the circuit as seen in Figure 1.6.

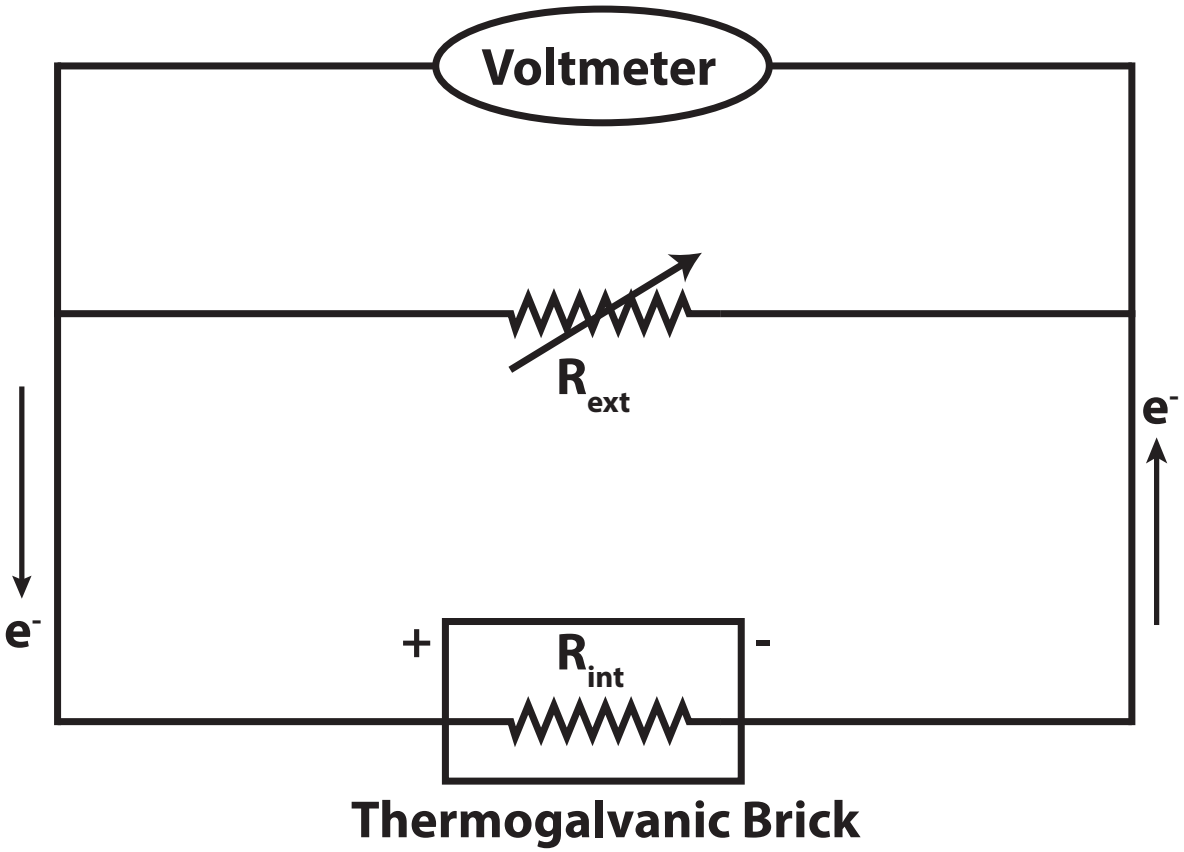

Figure 1.6: The Schematic Diagram of the Experimental Setup Using a Variable Resistor Switch Box of the Thermogalvanic Brick Circuit.

Rearranging equation 1.5 it is found that the current in the circuit is:

$$I = \frac{E}{R_{ext}} \tag{1.6}$$

which can then be applied to the Ohm's Law relation for power in a circuit (equation 1.4), thus giving:

$$P = \frac{E^2}{R_{ext}}. \tag{1.7}$$

The power output can also be related to the size of the electrode used by dividing the power by the electrode area to get:

$$P_{density} = \frac{P}{A_{electrode}} = \frac{P}{h_{electrode} \times w_{electrode}} \tag{1.8}$$

where $P_{density}$ is the power density, $A_{electrode}$ is the active area of the electrode, $h_{electrode}$ is the electrode active area height, and $w_{electrode}$ is the electrode active area width.

To compare power density across different ΔT the power density needs to be normalized by ΔT^2. Thus, the equation becomes:

$$P_{density,\Delta T} = \frac{P_{density}}{\Delta T^2} \tag{1.9}$$

where $P_{density,\Delta T}$ is the normalized power density and the change in temperature ΔT can be defined as:

$$\Delta T = T_h - T_c \tag{1.10}$$

where T_h is the temperature of the hot side electrode and T_c is the temperature of the cold side electrode.

An explanation for why the power density is normalized by dividing by ΔT^2 is from the relationship of current I within the thermoelectric device. In a thermoelectric (or thermogalvanic) device, the current through the device can be described as [38]:

$$I = \frac{\alpha \Delta T}{R_{int} + R_{ext}} \tag{1.11}$$

where α is the Seebeck coefficient which is described in equation 1.22. From equation 1.11 it can be determined that the power output of a thermogalvanic cell is directly related to ΔT^2 from combining equations 1.3, 1.4, and 1.11 as seen below:

$$P = \left(\frac{\alpha \Delta T}{R_{int} + R_{ext}}\right)^2 R_{ext}. \tag{1.12}$$

This relation shows that when normalizing the specific power density by ΔT^2 shown in equation 1.9, the resultant is the relationship between the Seebeck coefficient, and the internal and external resistances in a thermogalvanic brick. This allows for a way to compare thermogalvanic cell power density outputs across different ΔT values.

Furthermore, when applying equations 1.8 and 1.12 to equation 1.9, equation 1.9 can be rewritten to become:

$$P_{density,\Delta T} = \frac{P_{density}}{\Delta T^2} = \frac{\frac{\alpha^2}{(R_{int}+R_{ext})^2}R_{ext}}{A_{electrode}} \tag{1.13}$$

and because R_{ext} is equivalent to R_{int} at the maximum power output, equation 1.13 can be simplified to:

$$P_{density,\Delta T} = \frac{P_{density}}{\Delta T^2} = \frac{\left(\alpha^2/4R_{ext}\right)}{A_{electrode}}. \tag{1.14}$$

Therefore, the specific maximum power density output when normalized by ΔT^2 becomes a relationship of only the load resistance, R_{ext}, at the maximum power output, the Seebeck coefficient α, and the electrode active area $A_{electrode}$. Hence this removes the dependence on ΔT^2 from the maximum power output and provides a way to compare power density outputs of differing ΔT values.

Finally the maximum power output of a thermogalvanic cell can be described for cells with a linear relationship between cell potential and current by the following [20]:

$$P_{max} = \frac{1}{4}E_{oc}I_{sc} \tag{1.15}$$

where E_{oc} is the open circuit cell potential and I_{sc} is the short circuit current delivered by the cell. This maximum power can be simplified to:

$$P_{max} = \frac{E_{oc}^2}{4R_{int}} \tag{1.16}$$

where R_{int} is the internal resistance of the thermogalvanic cell (see Figure 1.6). Additionally, R_{int} is equivalent to R_{ext} when $P = P_{max}$, therefore the following relation can be formed [9]:

$$R_{int} = \frac{E_{oc}}{E}R_{ext} - R_{ext}. \tag{1.17}$$

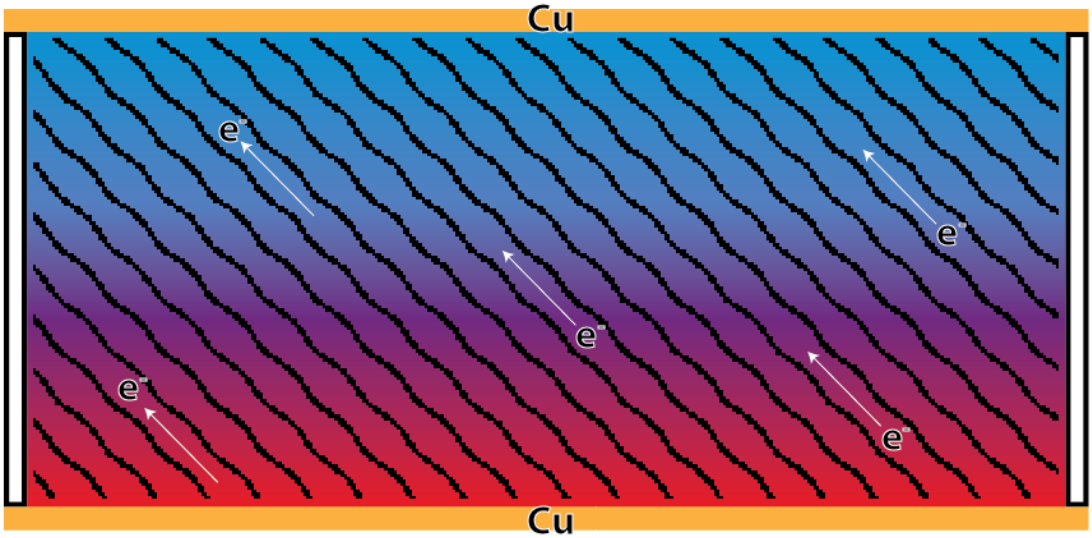

Figure 1.7: A Depiction of the Movement of electrons Through the Cross Section of an Aqueous $CuSO_4$ Electrolyte Thermogalvanic Brick with Copper Electrodes and a Schwartz D Inside.

The internal resistance of a thermogalvanic cell tells how the electrons and copper(II) ions move through the cell, as depicted in Figure 1.7. It has been determined that the internal resistances of a thermogalvanic cell are composed of three key components as follows [9]:

$$R_{int} = R_a + R_\Omega + R_m \tag{1.18}$$

where R_a is the activation resistance between the electrode and surface of the electrode, R_Ω is the ohmic resistance through the electrolyte, and R_m is the mass transfer resistance through the surface of the electrode. The activation resistance and ohmic resistance that make up the internal resistance of a thermogalvanic cell are defined as the following [9]:

$$R_a \equiv \left(\frac{\partial E}{\partial I}\right)_a = \frac{RT}{A_{s,electrode} n F j_o} \tag{1.19}$$

$$R_{\Omega} = \frac{L}{A_{s,electrode}\sigma} \tag{1.20}$$

where R is the universal gas constant, T is the absolute temperature, $A_{s,electrode}$ is the surface area of the electrode, n is the number of electrons involved in the redox reaction found in equation 1.23, F is the Faraday constant, j_o is the exchange current density, L is the electrode spacing, and σ is the ionic conductivity of the electrode. Unlike the activation resistance and ohmic resistance, the mass transfer resistance must be calculated using the experimentally measured R_{int} of the thermogalvanic cell by rearranging equation 1.18:

$$R_m = R_a + R_{\Omega} - R_{int}. \tag{1.21}$$

In the case of this thermogalvanic brick, the ohmic resistance through the bulk solution will need to take into account the resistance that the Schwartz D introduces to the brick when it is present. Currently there is not a mathematical equation that can exactly quantify the effect of this type of structure on the internal resistance, R_{int}, in a thermogalvanic cell, but it is hypothesized that the Schwartz D structure will increase the ohmic resistance as some of the paths through the structure are longer than without a Schwartz D (Figure 1.7).

1.3.3 Seebeck Coefficient

Although it is not within the scope of this project to evaluate the Seebeck Coefficient of the electrolyte, a general understanding is useful when dealing with thermogalvanic cells. The Seebeck coefficient is a way to relate the open circuit cell potential of a thermogalvanic cell to its temperature dependence [20]. The Seebeck coefficient of a thermogalvanic cell at steady state can be described mathematically as [9, 20]:

$$\alpha = \frac{\partial E}{\partial T} = \frac{(S_B + \hat{S}_B) - (S_A + \hat{S}_A) - n\overline{\overline{S}}_e}{nF} \tag{1.22}$$

where α is the Seebeck coefficient, S_B and S_A are the partial molar entropies of species B and A respectively, $\hat{S}_B$ and $\hat{S}_A$ are the Eastman entropies of the concerned species, F is the Faraday constant, $\overline{\overline{S}}_e$ is the total transport entropy in the metal electrodes, and n is the number of electrons involved in the redox reaction found in equation 1.23. The corresponding redox reaction for defining species A and B are as follows:

$$\mathrm{B} \rightleftharpoons ne + \mathrm{A} \tag{1.23}$$

1.3.4 Power Conversion Efficiency

Another important topic to understand that is outside the goals of this thesis is the power conversion efficiency of a thermoelectric device. The efficiency of a thermogalvanic cell can be described as [9]:

$$\eta_{max} = \frac{P_{max}}{\dot{Q}} \tag{1.24}$$

where η_{max} is the maximum thermogalvanic cell efficiency, P_{max} is the maximum power output of the cell, and $\dot{Q}$ is the heat flux through the cell.

Chapter 2

OVERVIEW OF DESIGN

This section outlines the initial design, the first prototype, the design revisions, the current prototype design, and the future design considerations.

2.1 Initial Design Requirements

The initial design requirements for the thermogalvanic brick were: have a thermogalvanic cell in the form of a UK metric brick at the size of $215\,mm \times 102.5\,mm \times 65\,mm$. The initial condition for the temperatures were to simulate a summer day in Arizona with the electrode temperatures at $T_h = 40°\text{C}$ and $T_c = 25°\text{C}$ as the cold side temperature giving a ΔT of 15°C. The chosen electrolyte and electrode combination was a 0.7 M $CuSO_4$ + 0.1 M H_2SO_4 aqueous electrolyte and Cu electrodes.

2.2 First Prototype Brick

The first prototype thermogalvanic brick was created using a full $0.22\,in$ thick acrylic casing with the outer dimensions meeting the $215\,mm \times 102.5\,mm \times 65\,mm$ size requirement. The copper electrodes were cut to fit inside the acrylic casing with 6 thermocouples placed along each of the sides of the acrylic walls of the brick (see Figure 2.1) for a total of 12 thermocouples. The insulation chosen was a pink fiberglass insulation which covers the 4 sides of the brick that were not parallel to the $0.6\,mm$ thick Cu electrodes.

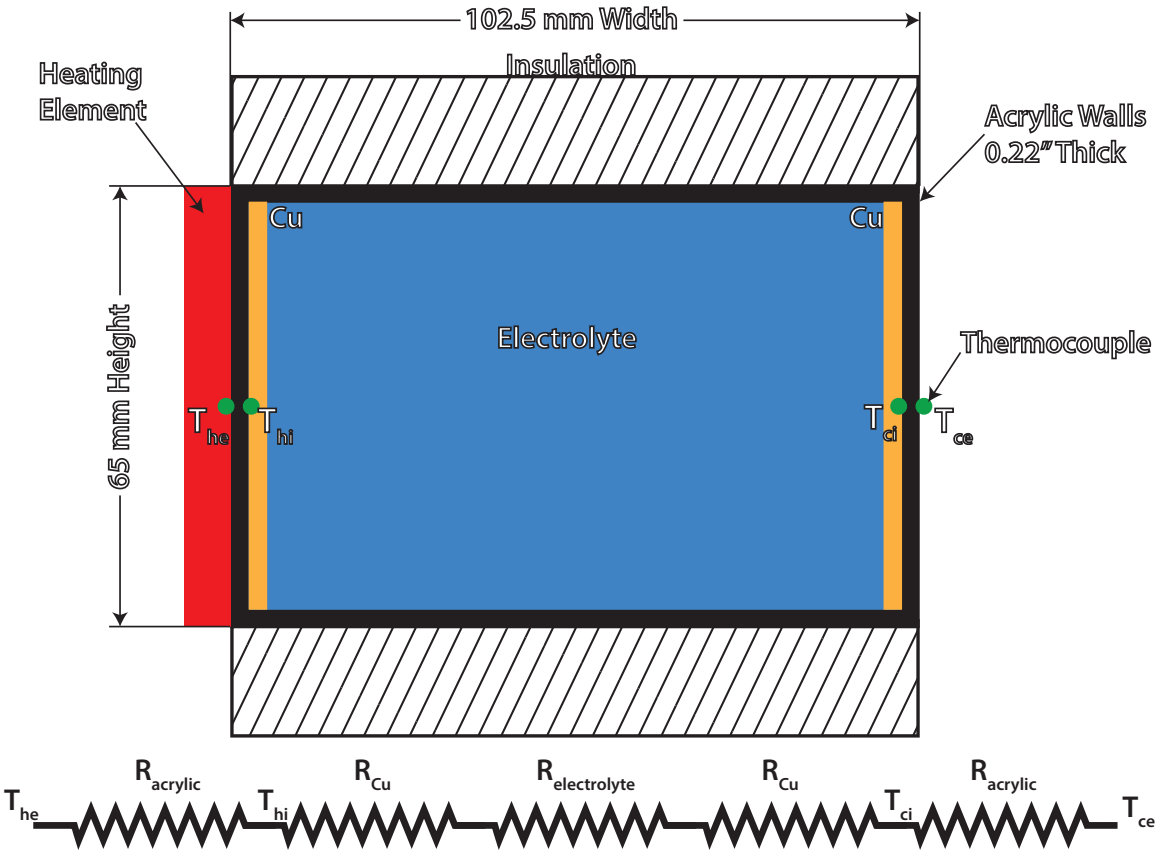

Figure 2.1: The 2D Cross Section of the Prototype Brick Showing Thermocouple Placement (with each Green Dot Representing 3 Thermocouples) as well as the 1D Conduction Thermal Resistance Circuit.

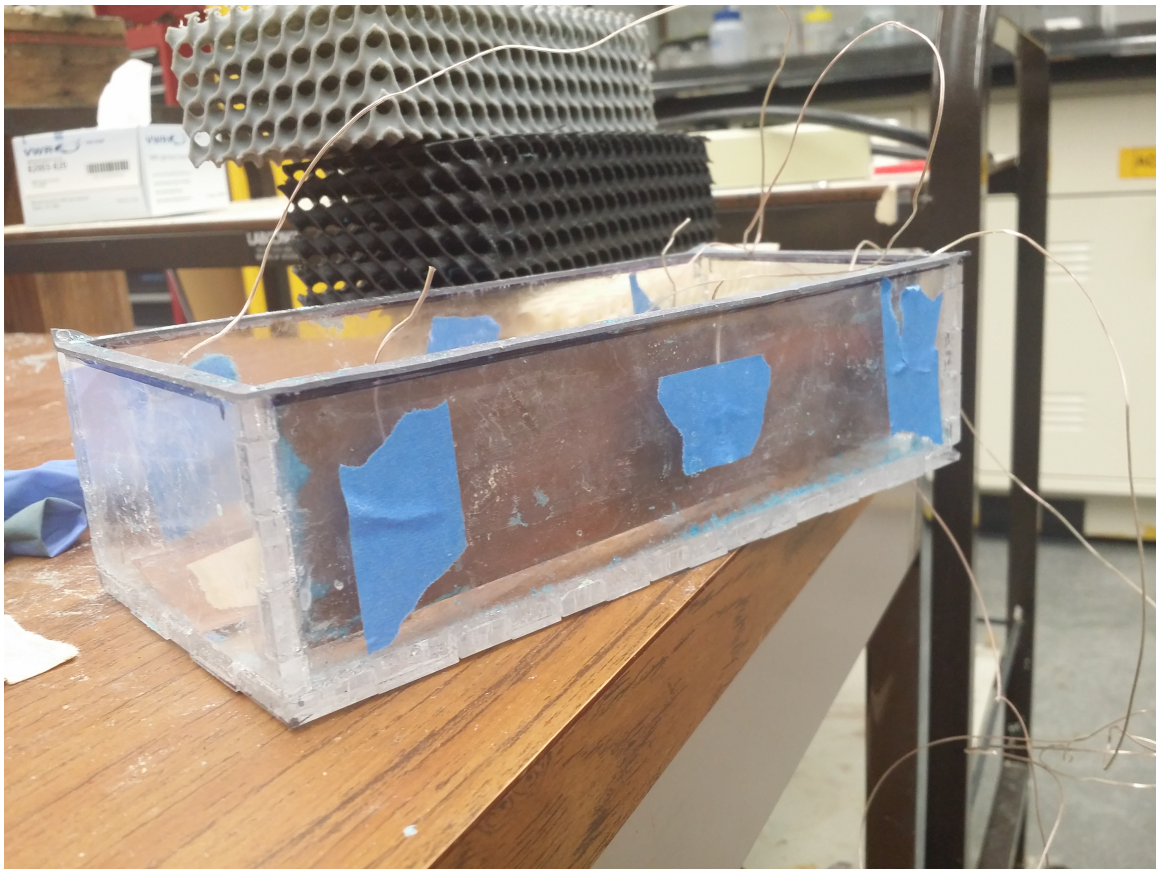

Figure 2.2: An Image of the De-lidded First Prototype Brick After Use.

This first prototype brick, seen in Figure 2.2, ended up yielding poor experimental results because of the thermally insulative nature of the acrylic walls. Using this first prototype yielded an external $\Delta T_{external}$ of around 15°C whereas the internal $\Delta T_{internal}$—which is critical to the performance of the thermogalvanic cell—was only around 3°C. $\Delta T_{external}$ and $\Delta T_{internal}$ are defined by equations 2.1 and 2.2:

$$\Delta T_{external} = T_{he} - T_{ce} \tag{2.1}$$

$$\Delta T_{internal} = T_{hi} - T_{ci} \tag{2.2}$$

Table 2.1: Table Showing the Thermal Conductivities and Resistances for the Prototype Brick.

	Thermal Conductivity, k $(\frac{W}{m \cdot K})$	**Thickness,** Δx **(mm)**	**Thermal Resistance, R** $(\frac{m^2 \cdot K}{W})$
Acrylic Wall	0.216	5.588	0.02587
Copper	386	0.6	1.5544e-6
Electrolyte	Approximately 0.6	90.124	0.1502
Total		102.5	0.20195

Using a simple 1D thermal resistance method for conduction, the following theoretical $\Delta T_{internal}$ was found to be 3.8°C.

For conduction the calculations for heat flux are as follows [39]:

$$\dot{Q} = \frac{\Delta T}{R_{th}} \tag{2.3}$$

where R_{th} is the thermal resistance between the points where ΔT is measured. The thermal resistance is defined as:

$$R_{th} = \frac{1}{u_{th}} \tag{2.4}$$

and

$$u_{th} = \frac{k}{\Delta x} \tag{2.5}$$

where u_{th} is the relationship between the thermal conductivity k and the thickness of the material Δx. Using the equations 2.3, 2.4, and 2.5 the values in Table 2.1 were calculated. These calculations proved why the design performed how it did in the initial experiment.

2.3 Design Revisions

Because of the very small ΔT between the Cu electrodes in the initial prototype brick, it was necessary to revise the design to get larger ΔT values between electrodes to boost the power output of the brick.

2.3.1 Potential Designs

To increase the ΔT between the two copper electrodes the amount of acrylic needs to be reduced. With that design feature in mind, a few options for the next prototype brick were created. The first, and most obvious design, was to completely remove two of the acrylic walls of the brick and replace them with copper that would serve as both the outer wall and the electrode. The other designs that arose through this were an acrylic wall with a rectangular hole in it to expose the copper electrode and a wall with an exposed diamond pattern as seen in Figure 2.3c.

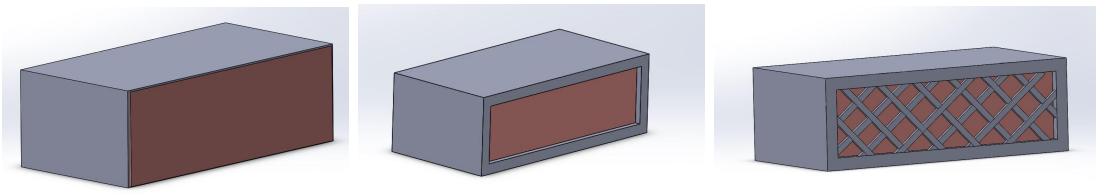

(a) Fully Exposed Electrode Walls

(b) Rectangular Cutout from the Walls

(c) Diamond Pattern Cutout from the Walls

Figure 2.3: Various Prototype 3D Models of the Brick.

The design with fully exposed electrodes (Figure 2.3a) gains the benefit of having potentially the highest ΔT between the electrodes because there is no air gap and no acrylic between the heating element and the electrode. On the other hand, the design in Figure 2.3c will gain added structural stability from the acrylic wall—which is most likely not needed since the load applied to the brick should mostly be supported

by the minimal surface Schwartz D internal to the brick—at the cost of potentially reducing the amount of heat that can be transfered into the electrode.

2.4 Current Prototype Design

A variation of the design in Figure 2.3a was chosen as the design for the results presented in this thesis. The exposed nature of the electrodes allows for the brick to have the greatest potential ΔT of the presented designs in 2.3. The internal size of the brick was chosen to match the internal size of a brick with full $0.22\,in$ acrylic walls. This would mean the brick is slightly smaller (as seen in Figure 2.4) than $215\,mm \times 102.5\,mm \times 65\,mm$ with a size of $215\,mm \times 92.524\,mm \times 65\,mm$ using $0.6\,mm$ thick copper walls. This would mean the same electrode spacing and Schwartz D structures could be used for the current and future experiments.

The copper electrodes were also chosen to be slightly larger than the $215\,mm \times 65\,mm$ area of a standard metric brick to make the manufacturing and testing of the brick easier. The copper plate size used to create the wall was $228.6\,mm \times 76.2\,mm$.

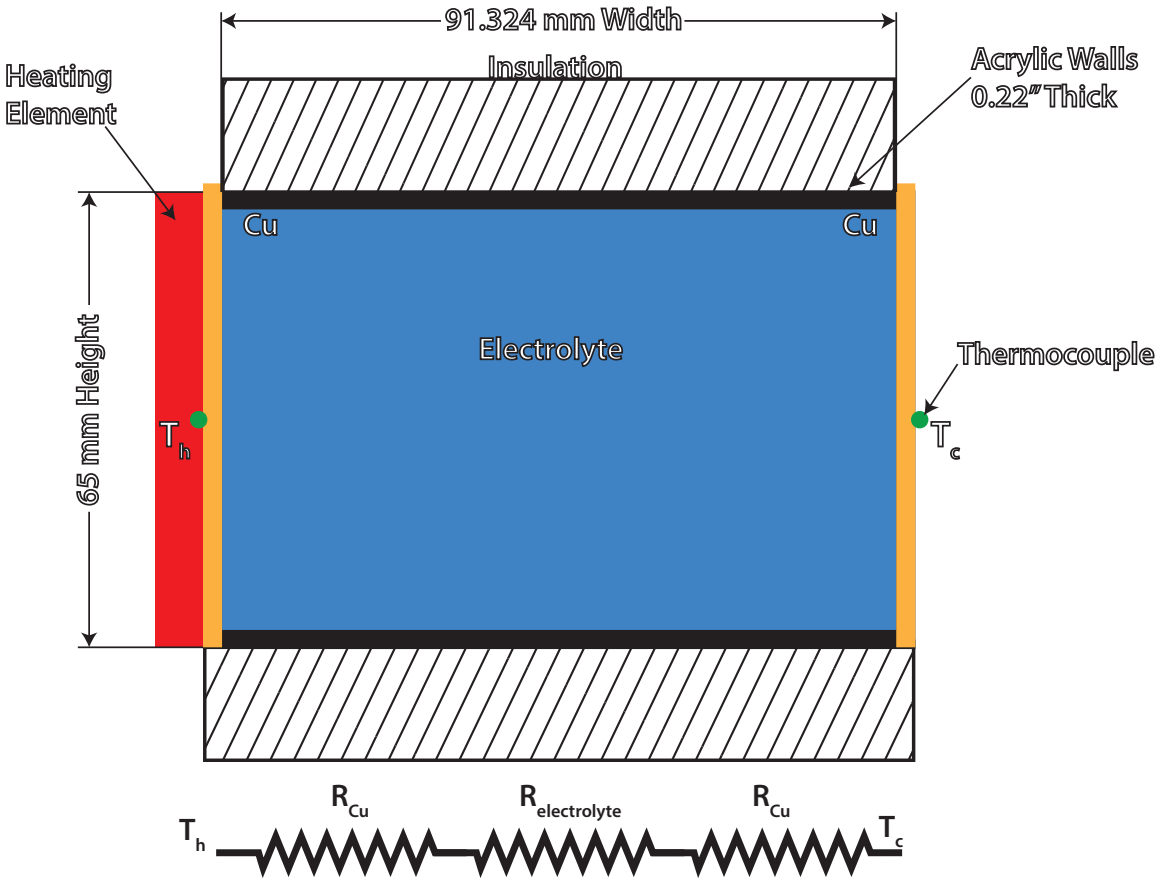

Figure 2.4: The 2D Cross Section of the New Prototype Brick Showing Thermocouple Placement (With Each Green Dot Representing 3 Thermocouples) as well as the 1D Conduction Thermal Resistance Circuit.

2.5 Future Design Considerations

The design in Figures 2.3c and 2.5 is taken for future consideration as it will add some protection to the copper as well as not require the copper electrode to be $0.22\,in$ (or $5.588\,mm$) thick to meet the UK metric brick size. Along with adding protection to the sides of the brick, it would also provide extra structural stability to the brick. A future consideration for this design would also be to fill in all the air gaps with thermally conductive epoxy to create a path for heat to transfer to the hot side of

the electrode.

Another consideration would be to use the design in Figure 2.3b and fill the cavity with thermally conductive epoxy to get even better thermal conductivity than that found in the design in Figure 2.3c.

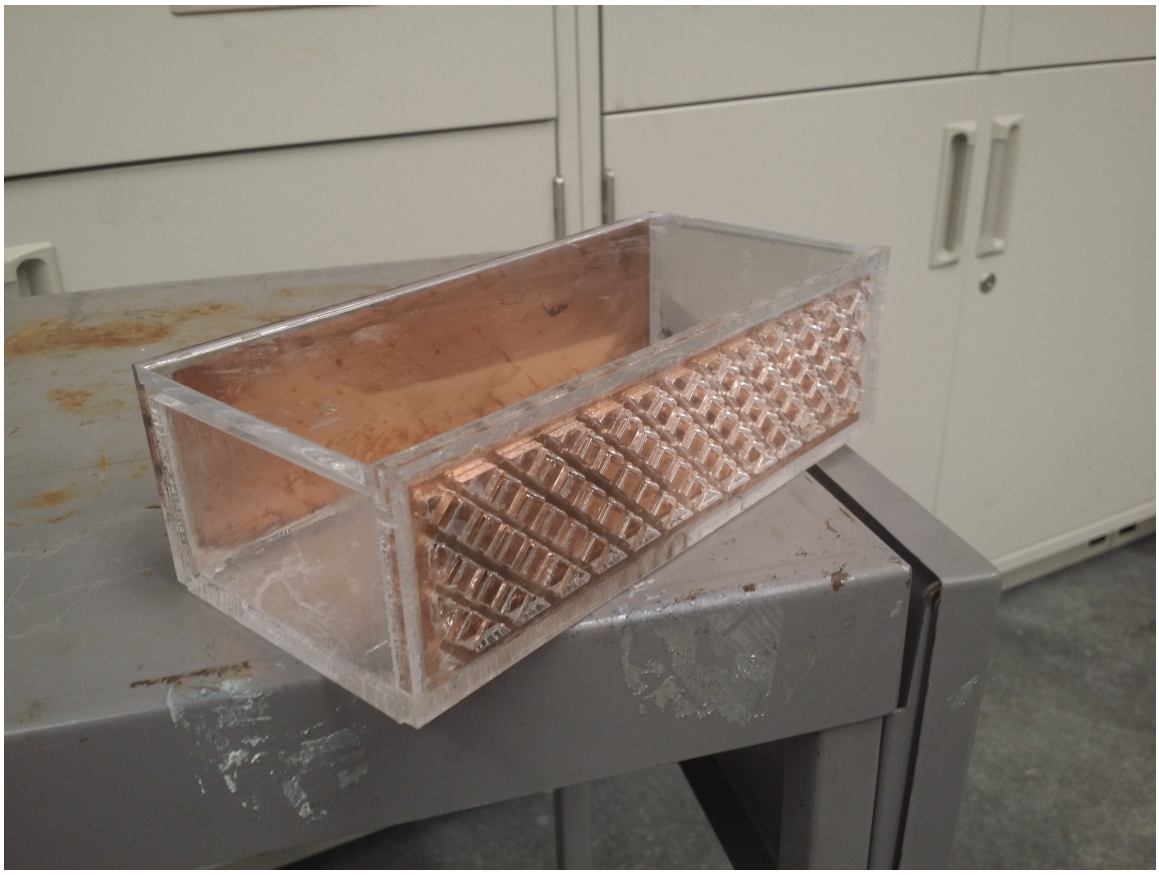

Figure 2.5: An Image of a Potential Future Brick Design Following the Diamond Cutout in Figure 2.3c

.

Chapter 3

PHYSICAL SYSTEM

This chapter will cover the required parts and materials of the physical thermogalvanic brick as well as the equipment required for the experiment.

3.1 Materials

The materials required for building the physical system are found in Table 3.1. Table 3.1 includes items both purchased and already present in the lab used in the experiment. The 3D printing filaments used were: ABS, Polycarbonate-ABS (PCABS), and Polycarbonate-Carbon Fiber (PCCF). Likewise, Table 3.2 shows the necessary equipment used in the experimental setup with Figure 3.1 showing the front panels of the Fluke electrometer and Tektronix DC power supply.

Table 3.1: Table of the Bill of Materials Used in this Project.

Item	**Detailed Description**	**Supplier**	**Size**	**Qty.**
DI Water	Deionized Water	ASU Chemistry Lab Supply	$1\,gallon$	2
Copper	Pure Copper	Industrial Metal Supply	12" × 12" × 0.023622"	1
Sulfuric Acid	H_2SO_4, ACS Grade $CAS\#7664-93-9$	AMRESCO	$500\,mL$	1
Copper (II) Sulfate Pentahydrate	$CuSO_4{\cdot}5H_2O$ 99% $CAS\#7758-99-8$	PTI Process Chemicals	$2.5\,kg$	1
Thermocouple	K Type	Omega	$1\,m$ Length	6
Wire	20 Gauge	Standard	$1\,m$ Length	4
Beaker	Glass	Pyrex	$500\,mL$	2
Graduated Cylinder	Glass	Pyrex	$500\,mL$	1
Strip Heater	$300\,W$	McMaster Carr	10" × 3"	1
Acrylic Sheet	0.22" Thick	Home Depot	24" × 36"	1
Nitrile Gloves	Chemical Resistant	Deal Med	Standard	1
Sandpaper	220 Grit and 600 Grit	3M	Standard	1
Resistors	$1\,\Omega$ to $1000\,\Omega$	Digikey	Standard	1 each
Fiberglass Insulation	$1\,in$ Thick Minimum	Home Depot	Large Roll	1
3D Printing Filament	ABS, PCABS, PCCF	Zortrax (ABS, PCABS), PRILINE (PCCF)	$1\,kg$	1 each
Heat Sink Compound	340 Silicone	DOW Corning	$142\,g$	1

Table 3.2: Table of Equipment Needed to Perform the Experiments.

Equipment	**Model**	**Manufacturer**	**Quantity**
cDAQ	9171	NI	1
DAQ Thermocouple Module	9213	NI	1
Electrometer	8846A	Fluke	1
Programmable DC Power Supply	PS2520G	Tektronix	1
Computer	With LabVIEW	Any	1
Liquid CPU Cooler	Seidon 120V	Cooler Master	1
Pump	Water Pump	Any	1
3D Printer	M200	Zortrax	1

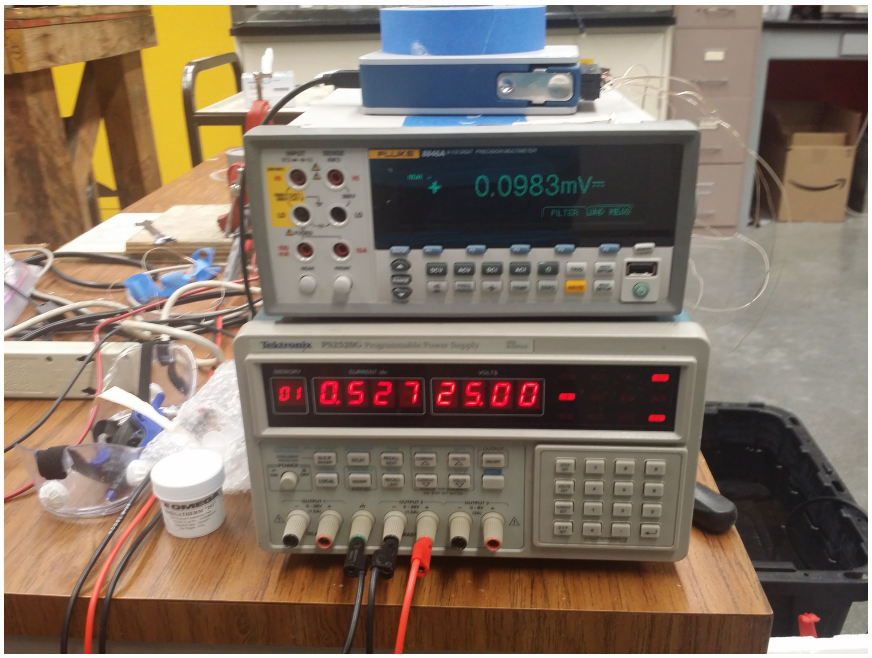

Figure 3.1: From Top to Bottom, the NI-cDAQ 9171, the Fluke 8846A and the Tektronix PS2520G Used in the Experiment.

3.3 System Layout

The physical system layout is shown below in Figures 3.2 and 3.3. A schematic diagram of the whole system can be found in Figure 4.2.

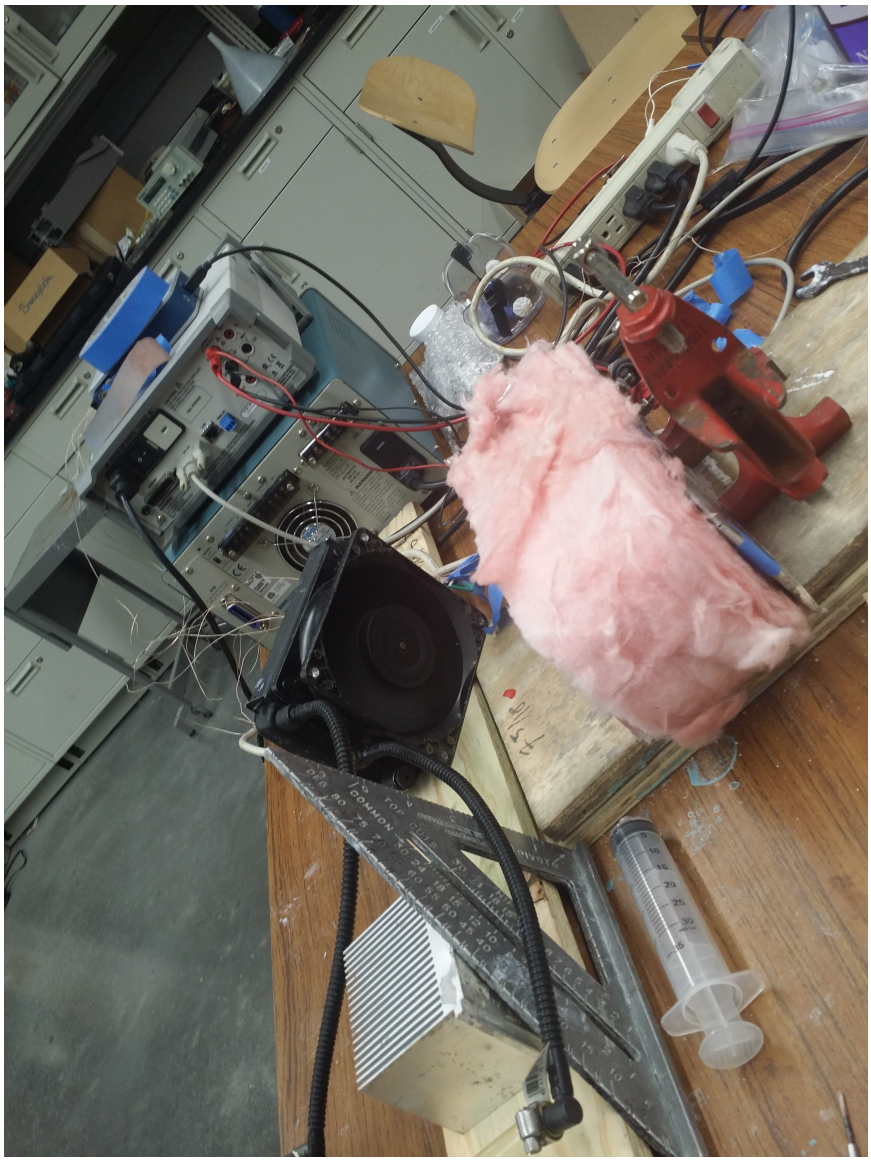

Figure 3.2: Image Showing the Side of the Physical Setup of the Experiment.

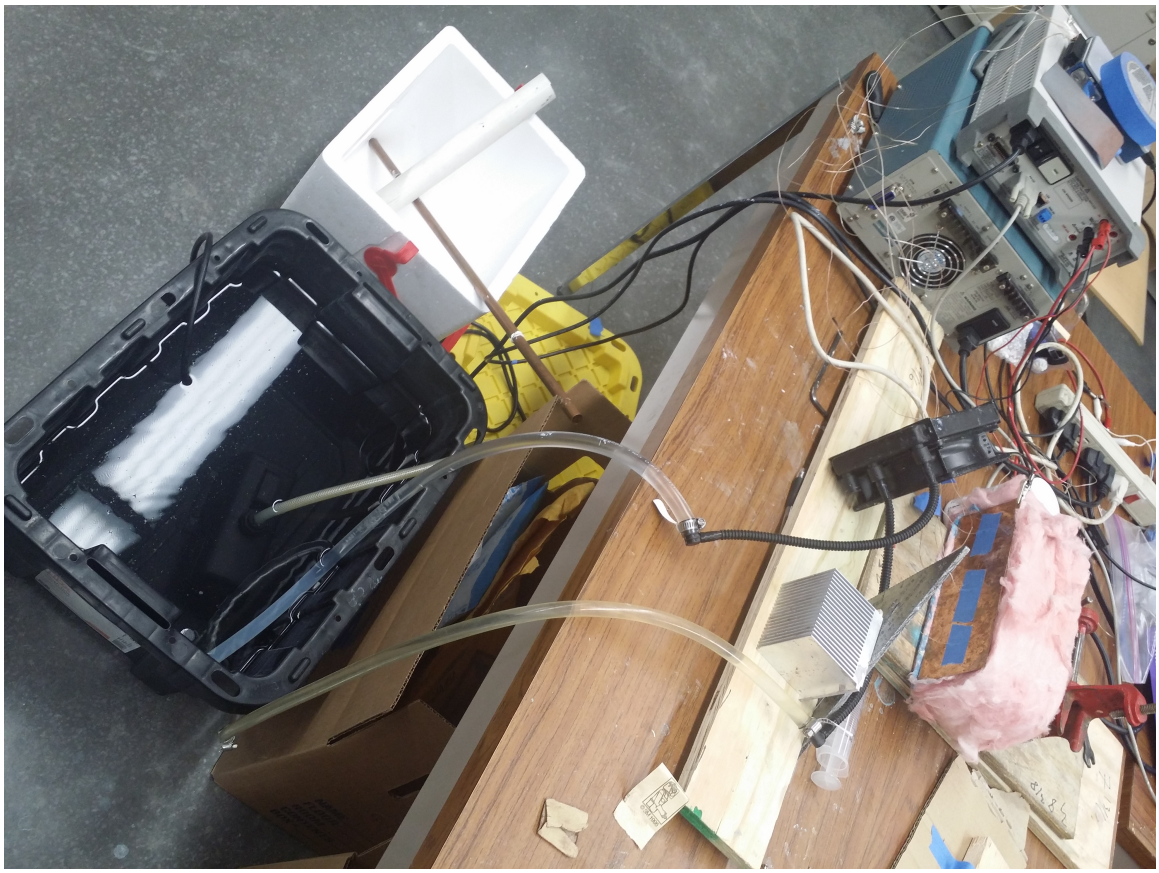

Figure 3.3: Image Showing the Physical Setup of the Experiment including the Water Cooling Pump and Water Reservoir.

Chapter 4

EXPERIMENTAL PROCEDURES

The experimental procedures will be outlined in this chapter spanning from the preparation of the electrolyte to the experimental procedure for measuring the power output of the thermogalvanic brick.

4.1 Electrolyte Synthesis

The target concentration of 0.7 M $CuSO_4$ + 0.1 M H_2SO_4 aqueous electrolyte was created by first dissolving the $CuSO_4{\cdot}5H_2O$ salt crystals into deionized water. Once the blue crystals were fully dissolved, the necessary amount of ACS grade ($\geq$ 95% purity) H_2SO_4 was slowly mixed into the solution. After the acid was added to the mixture, more deionized water was added to the mixture until the correct 0.7 M $CuSO_4$ + 0.1 M H_2SO_4 concentration of electrolyte was achieved. The thermogalvanic brick requires approximately 1 L of electrolyte, thus 500 mL batches of the electrolyte were made 2 at a time to fulfill the electrolyte requirement of the brick. A note on the copper electrodes: the geometric active area for the electrodes was approximately 105.69 cm^2.

4.2 Resistor Preparation

Prior to the experiment, each of the resistors and wires that were used in the experiment were tested using the Fluke 8846A 4-wire resistance test function to get a more accurate measure of the exact resistance applied as load. By doing so, the accuracy of the current measurements will also be affected.

4.3 Experimental Setup

Before any experiment was performed, the copper electrodes were first cleaned and polished to remove any oxidation or residue left on the copper. Each electrode was first rinsed with water, dried, then sanded with 220 grit sand paper and polished using 600 grit sand paper. After the polishing was completed, the electrodes were once again rinsed with water and dried. After drying the electrodes were washed once more using alcohol and dried once more to ensure all the copper powder produced from the sanding and polishing was completely removed.

After the cleaning process, the Omega K type thermocouples were attached to the outside of the electrodes, 3 per side. The opposite thermocouple ends were connected to an NI-9213 thermocouple module coupled with an NI cDAQ-9171 chassis which was connected through USB to the computer for data logging. Next, the strip heater was attached to the Tektronix PS2520G programmable DC power supply unit and attached to the hot side electrode using a thermal interface material of DOW 340 Silicone Heat Sink Compound. After connecting the heater to the hot side of the thermogalvanic brick, the water pump and liquid cooling radiator were set up on the cold side. The Fluke 8846A was then connected to the copper electrodes of the brick in parallel to the variable resistance as seen in Figure 4.1.

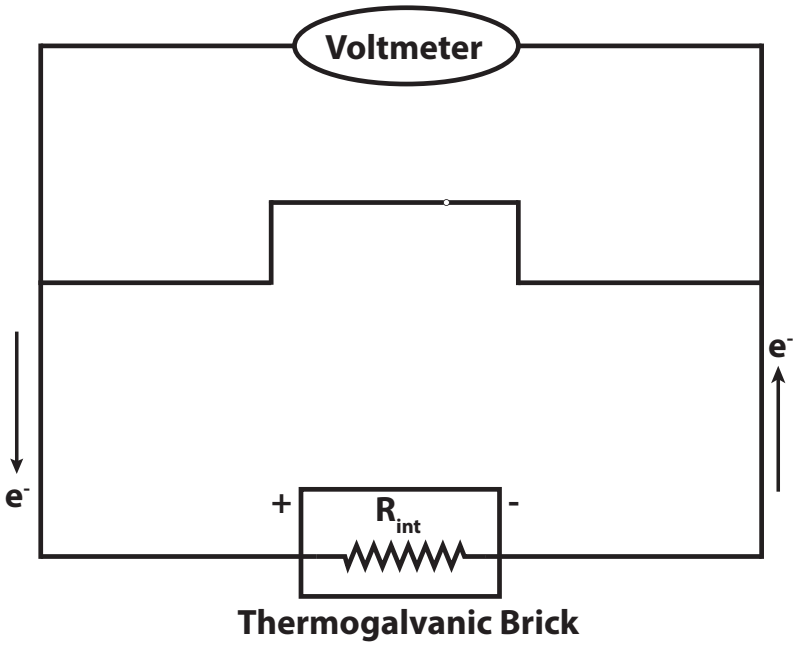

Figure 4.1: The Schematic Diagram of the Experimental Setup of the Thermogalvanic Brick Circuit With the Switch in the Closed Configuration and the Resistor Removed.

Once the circuit was setup in the configuration shown in Figure 4.1, the Schwartz D structure (if required) was placed inside the brick. With the required Schwartz D in place, the brick was then filled with electrolyte (approximately $750\,mL$) until full. Next, the Tektronix Power Supply was set to output $25\,V$ to the strip heater and the radiator fan and water cooler pump were powered up. Data recording using LabVIEW was started for collecting the thermocouple and cell potential data from the NI cDAQ and the Fluke Electrometer. See Figure 4.2 for a full diagram showing the experimental setup.

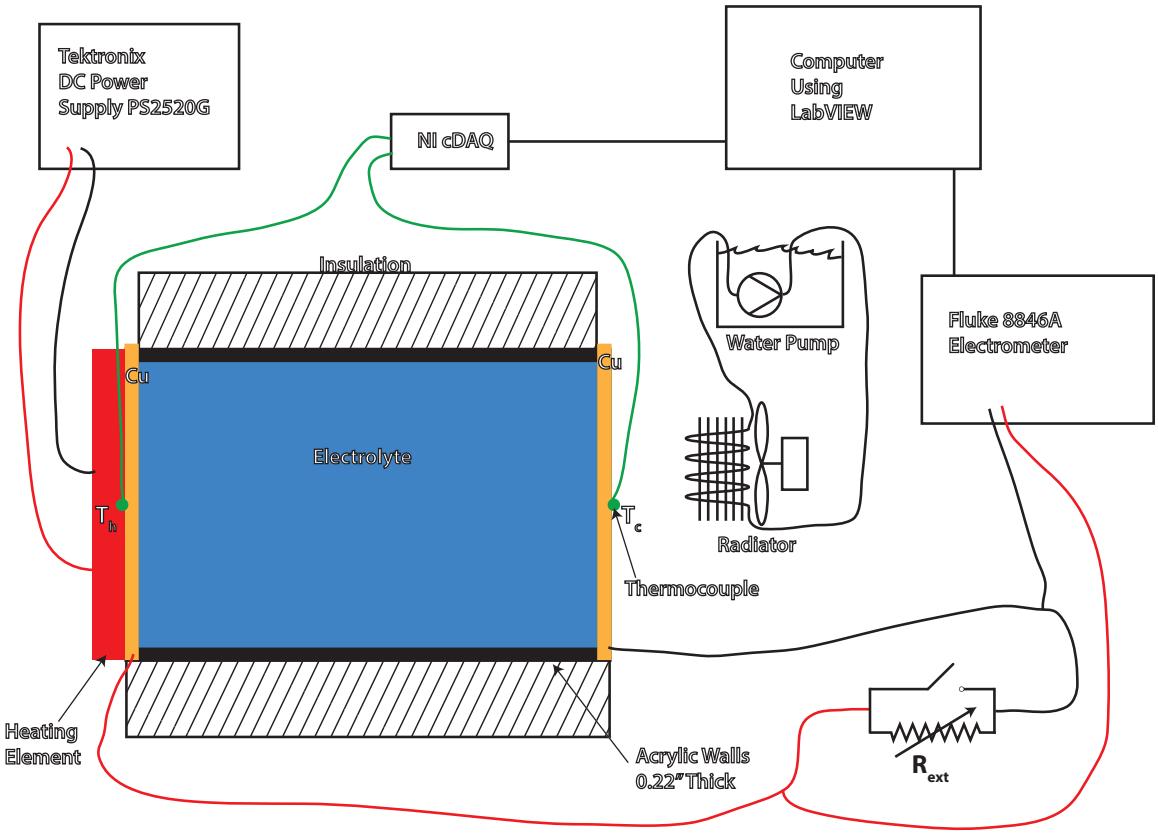

Figure 4.2: The Full Schematic Diagram of the Experimental Setup where the Green Dot Represents 3 Thermocouples.

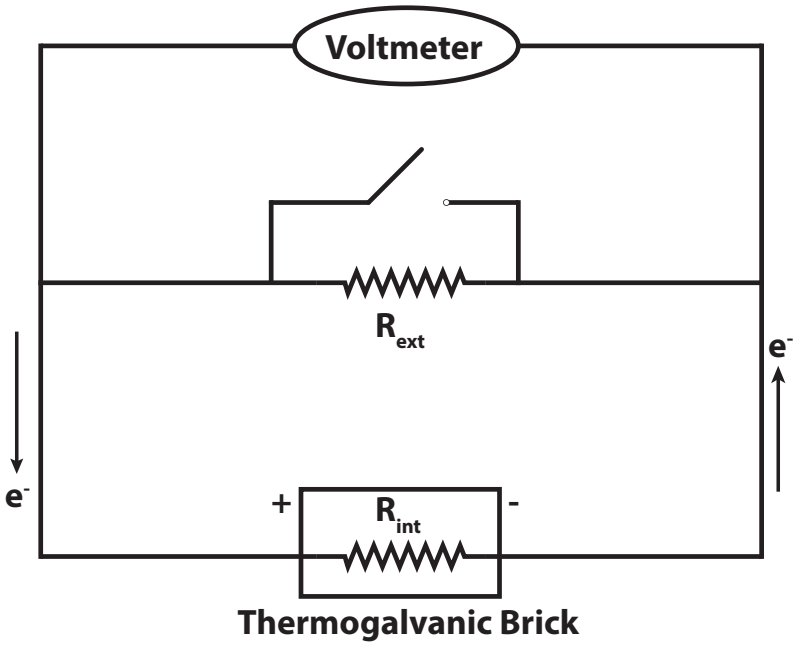

Figure 4.3: The Schematic Diagram of the Experimental Setup of the Thermogalvanic Brick Circuit With the Switch Open Applying the Load R_{ext}.

4.4 Experimental Procedure

The data recording was set in the LabVIEW VI to record one sample of cell potential per second with the sampling of temperature data much higher at 100 samples a second. After data recording was started, DC voltage was supplied to the heater, and the cooling unit was turned on, the system requires a waiting period to reach steady state. The time required for the system to reach steady state was about 3 to 4 hours. It was especially long since the volume of electrolyte was significantly large, at $1\,L$. After reaching steady state, the resistors were attached to the circuit and the switch was flipped to the open position shown in Figure 4.3. The switch was then closed and the resistor was removed.

This process was repeated starting at $1\,\Omega$ ascending to $1000\,\Omega$, repeated at $1000\,\Omega$ descending to $1\,\Omega$, and repeated for randomly ordered resistances testing each resistor

between $1\,\Omega$ and $1000\,\Omega$. Once this process was completed, the data recording was stopped, the voltage output from the Tektronix power supply to the strip heater was turned off, and the pump and radiator fan were unplugged. The Schwartz D structure was then removed from the brick (if required) and the electrolyte was emptied into the chemical waste area. The process then starts from the cleaning and polishing of the copper electrolyte to perform the experiment again.

Chapter 5

DISCUSSION AND RESULTS

Following the experimental procedures outlined in Chapter 4 the experiments to find power output for electrolyte only, ABS Schwartz D, PCABS Schwartz D, and PCCF Schwartz D were performed. All the results discussed here refer to the thermogalvanic brick with full copper walls. Only the plots discussed in the text will appear in this section; for the full list of figures from the experimental results, refer to Appendix A.

5.1 Experimental Results

5.1.1 Initial Experimental Results for the Copper Walled Brick

The initial acceptable results that follow the trends and magnitudes found in previous literature for thermogalvanic cells are outlined in this section.

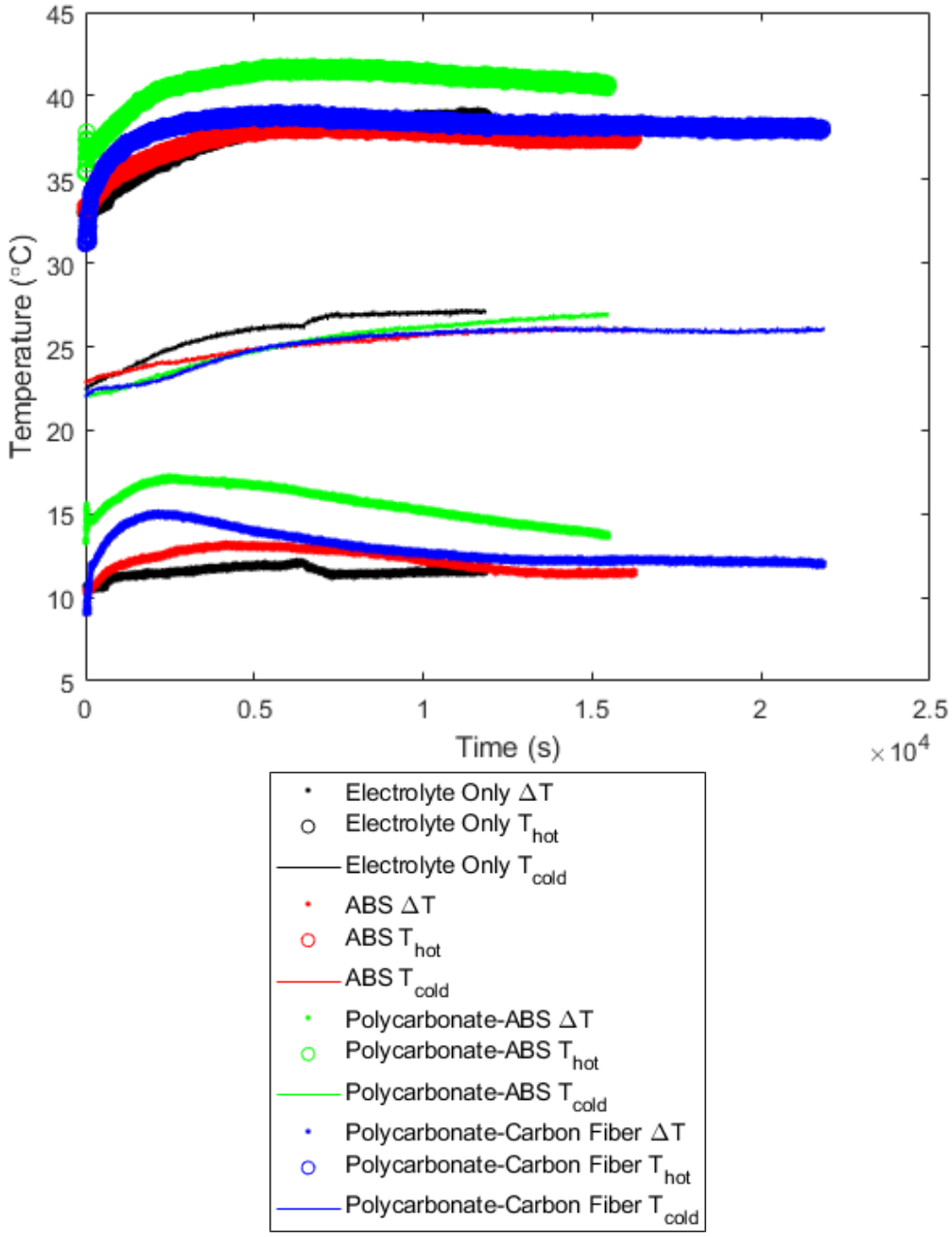

Figure 5.1: Plot of Temperature vs Time for the Experiments on the Thermogalvanic Brick for the Initial Experiments.

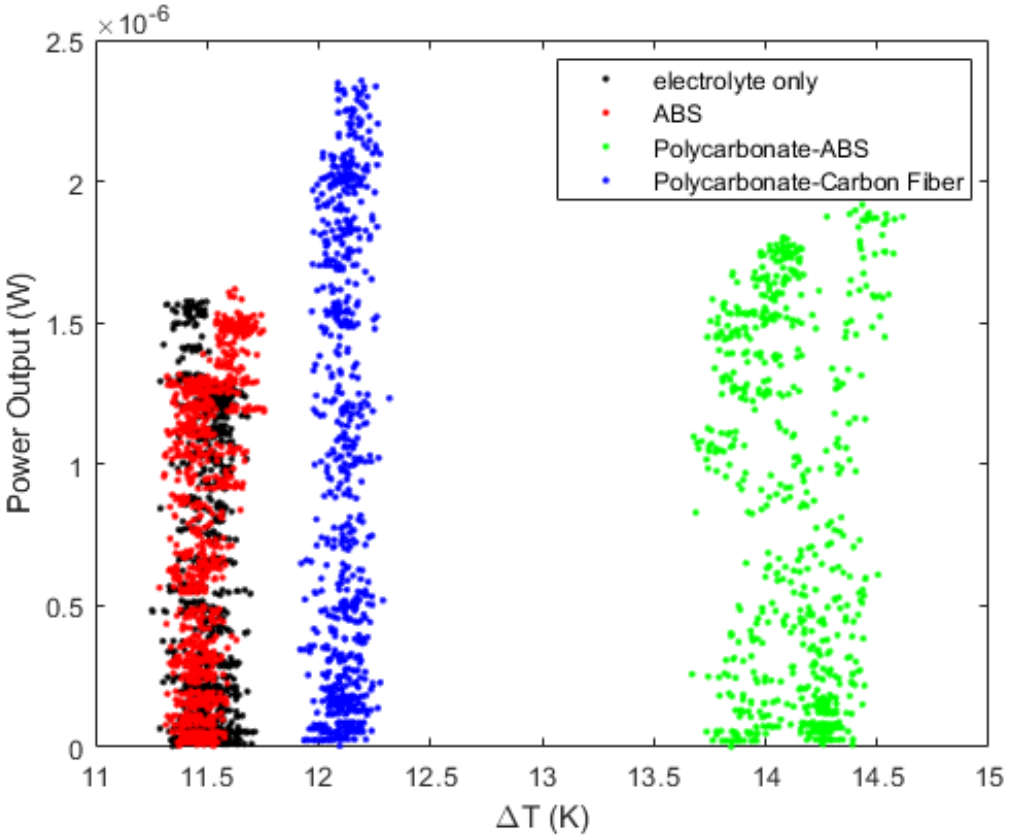

Figure 5.2: A Comparison of Power Output of the Thermogalvanic Brick across ΔT for the Different Schwartz D Materials for the Initial Experiments.

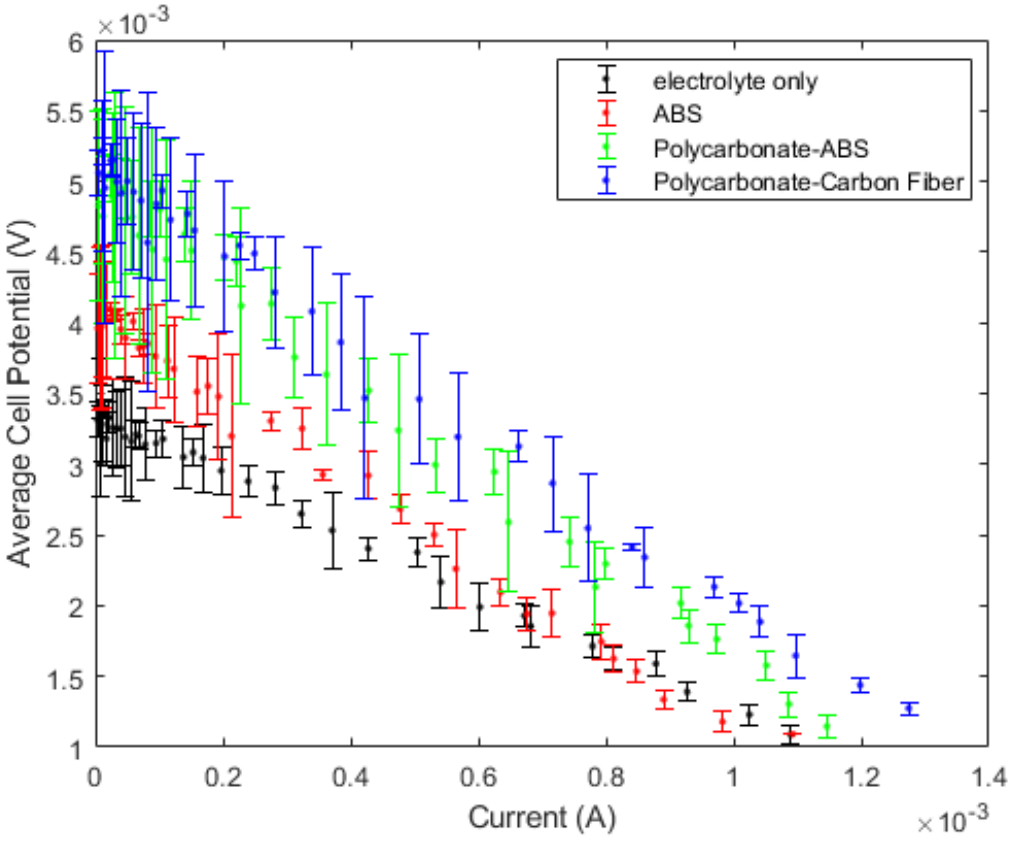

Figure 5.3: A Plot Showing Average Cell Potential Vs Current with Calculated Error Bars for the Initial Experiments.

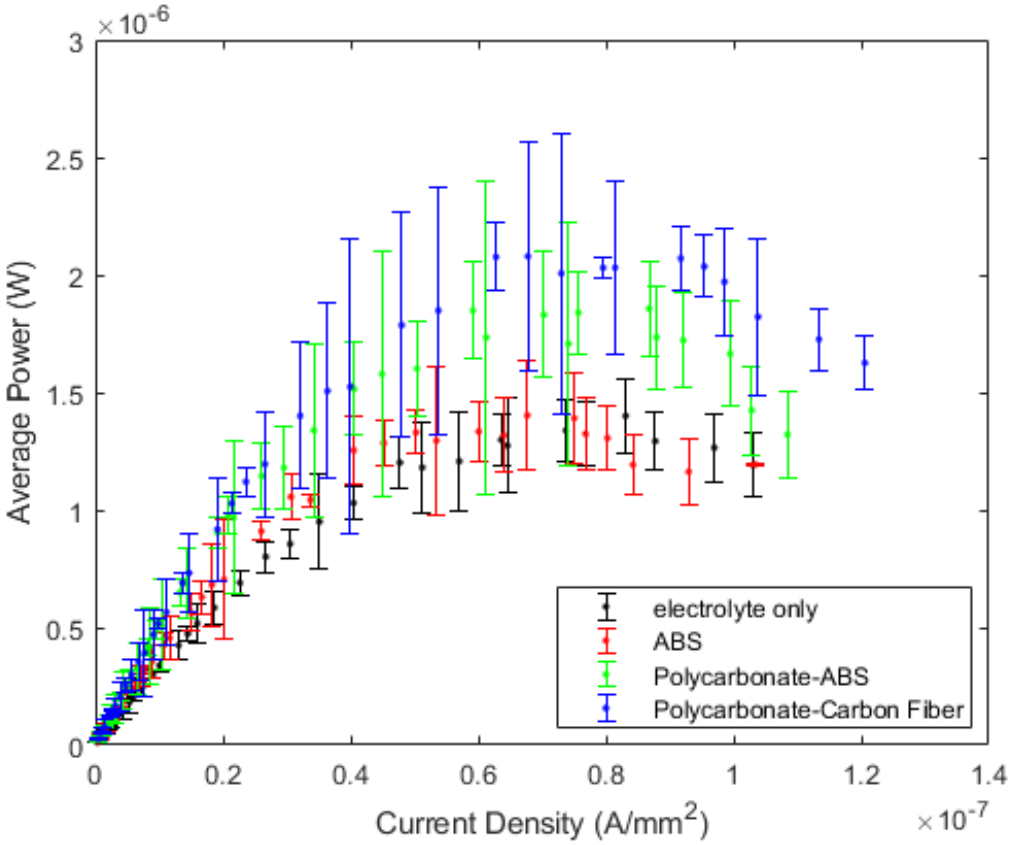

Figure 5.4: A Plot Showing The Power Output of the Thermogalvanic Bricks vs Current Density with Calculated Error Bars for the Initial Experiments.

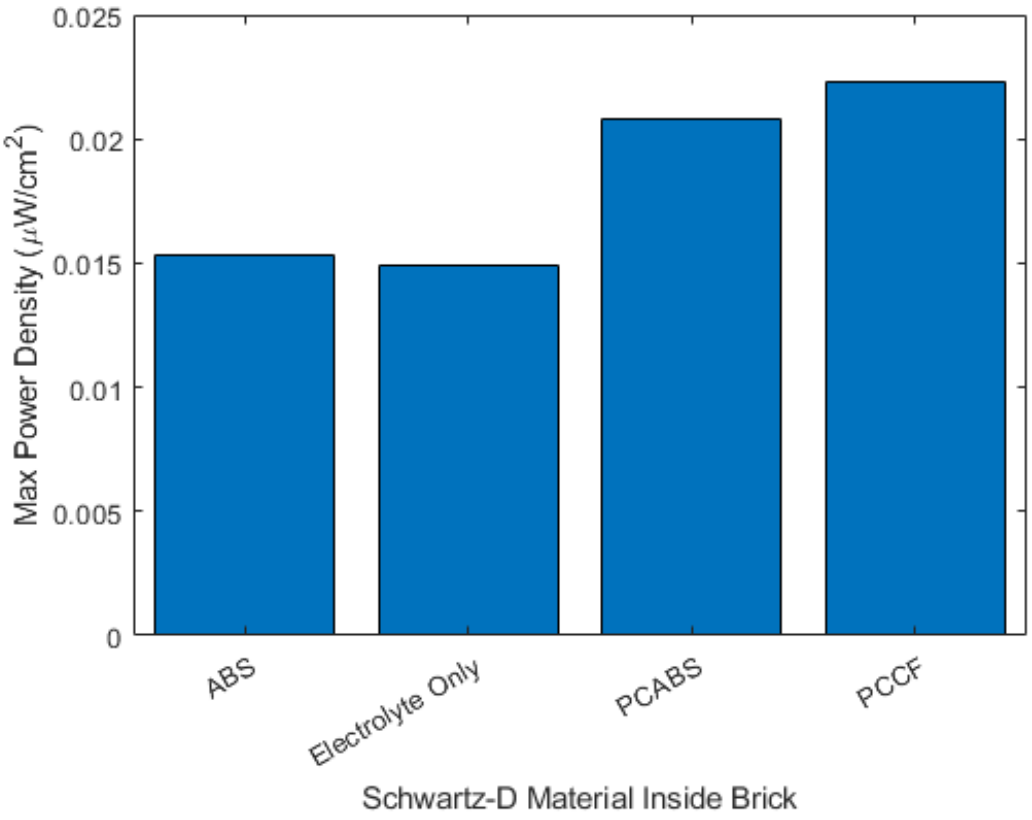

Figure 5.5: A Comparison of the Maximum Power Output for a Thermogalvanic Brick Containing Different Schwartz D Materials for the Initial Experiments.

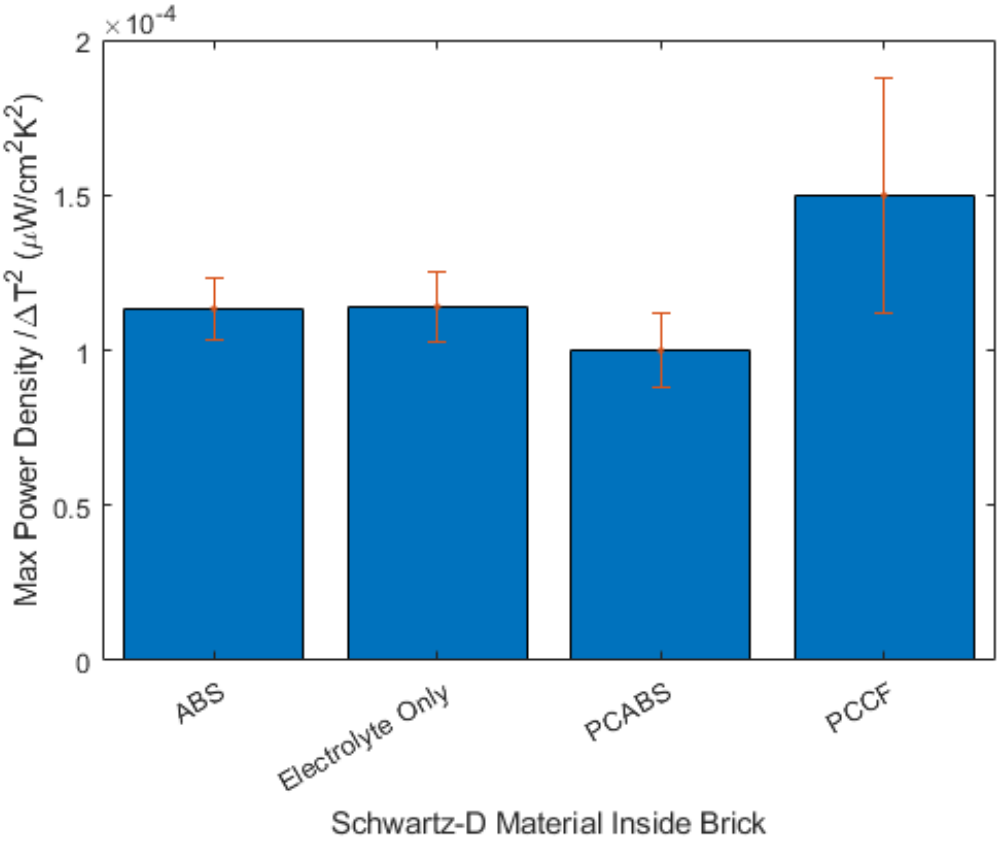

Figure 5.6: A Comparison of the Temperature Normalized Maximum Power for a Thermogalvanic Brick Containing Different Schwartz D Materials with Calculated Error Bars for the Initial Experiments.

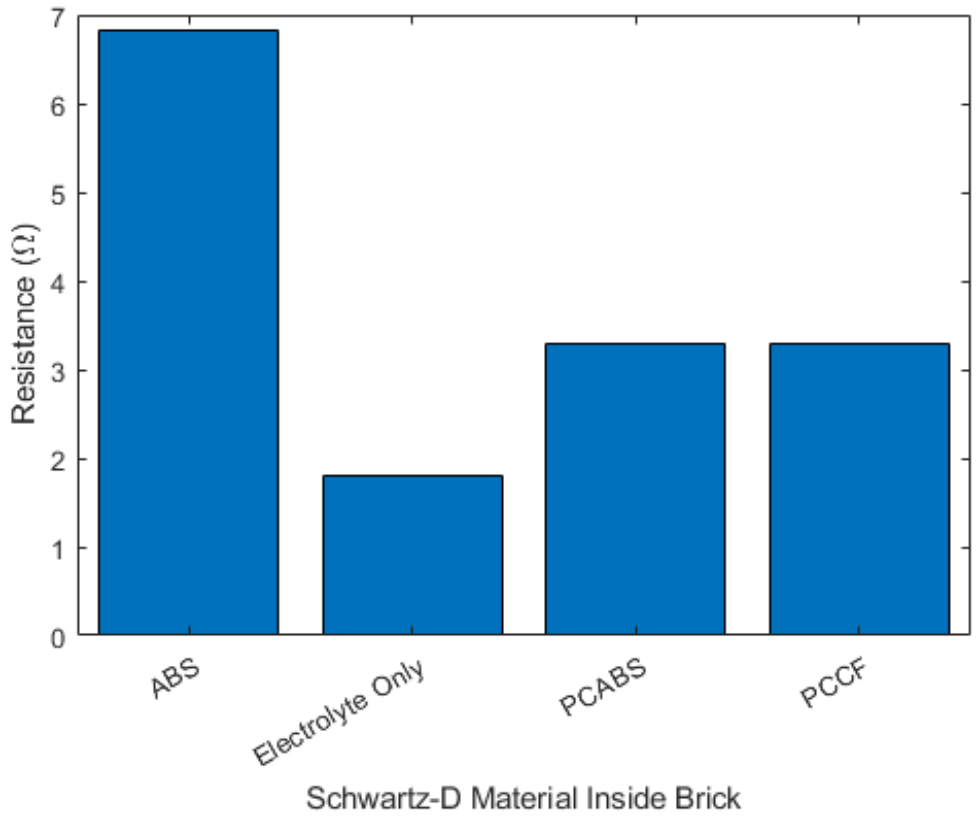

Figure 5.7: A Comparison of the Resistance Values at which the Maximum Power Density Output of the Thermogalvanic Cell were Found for a Thermogalvanic Brick Containing Different Schwartz D Materials for the Initial Experiments.

Table 5.1: Tabulated Values of Maximum Power Output and Temperature Normalized Maximum Power Output for the Initial Experiments.

	Electrolyte Only	**ABS**	**PCABS**	**PCCF**
Max Power Density Output ($\frac{\mu W}{cm^2}$)	0.01491	0.01532	0.02081	0.02229
Max Normalized Power Density Output ($\frac{\mu W}{cm^2 \cdot K^2}$)	1.1408×10^{-4}	1.1335×10^{-4}	0.9981×10^{-4}	1.4994×10^{-4}

5.1.2 Validation Experimental Results for the Copper Walled Brick

The experiments to gather the results and data outlined in the previous subsection 5.1.1 were performed again to validate the data and reduce the uncertainty found in the power output. The results are as follows.

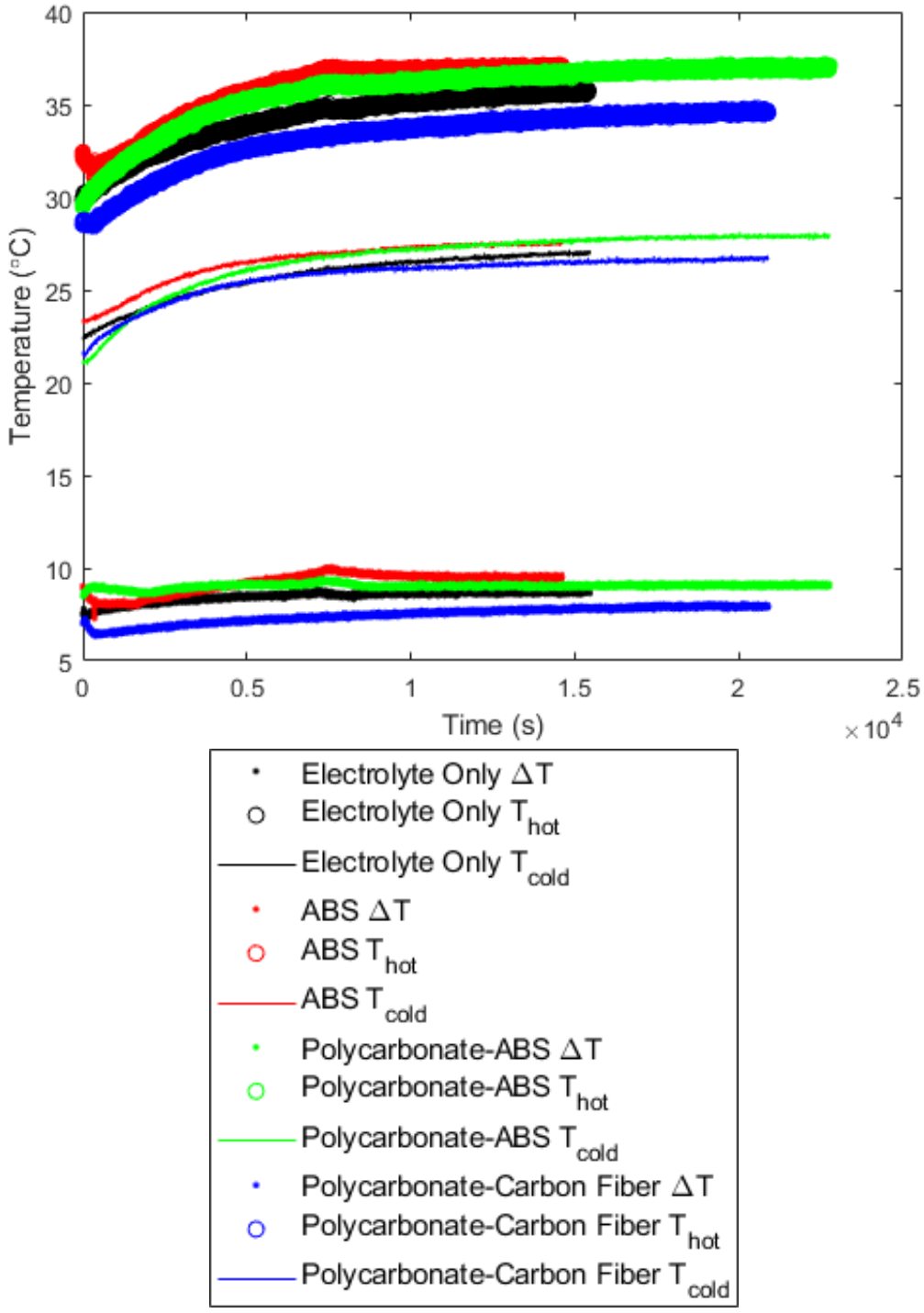

Figure 5.8: Plot of Temperature vs Time for the Experiments on the Thermogalvanic Brick for the Validation Experiments.

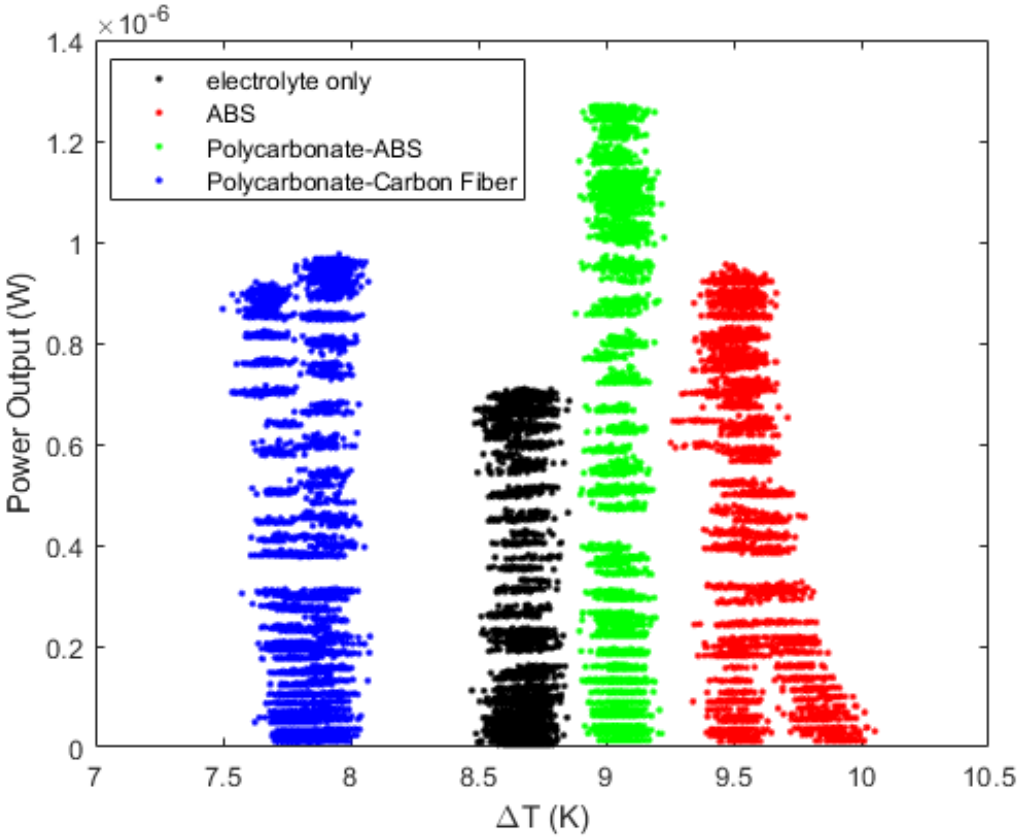

Figure 5.9: A Comparison of Power Output of the Thermogalvanic Brick across ΔT for the Different Schwartz D Materials for the Validation Experiments.

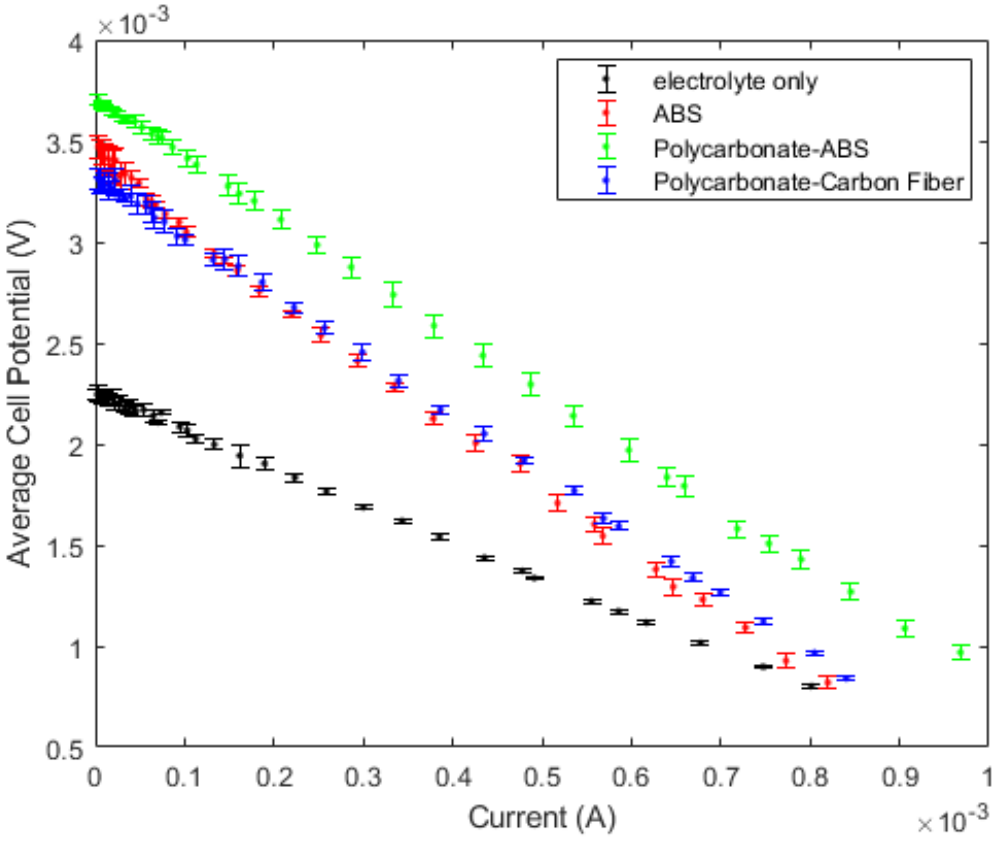

Figure 5.10: A Plot Showing Average Cell Potential Vs Current with Calculated Error Bars for the Validation Experiments.

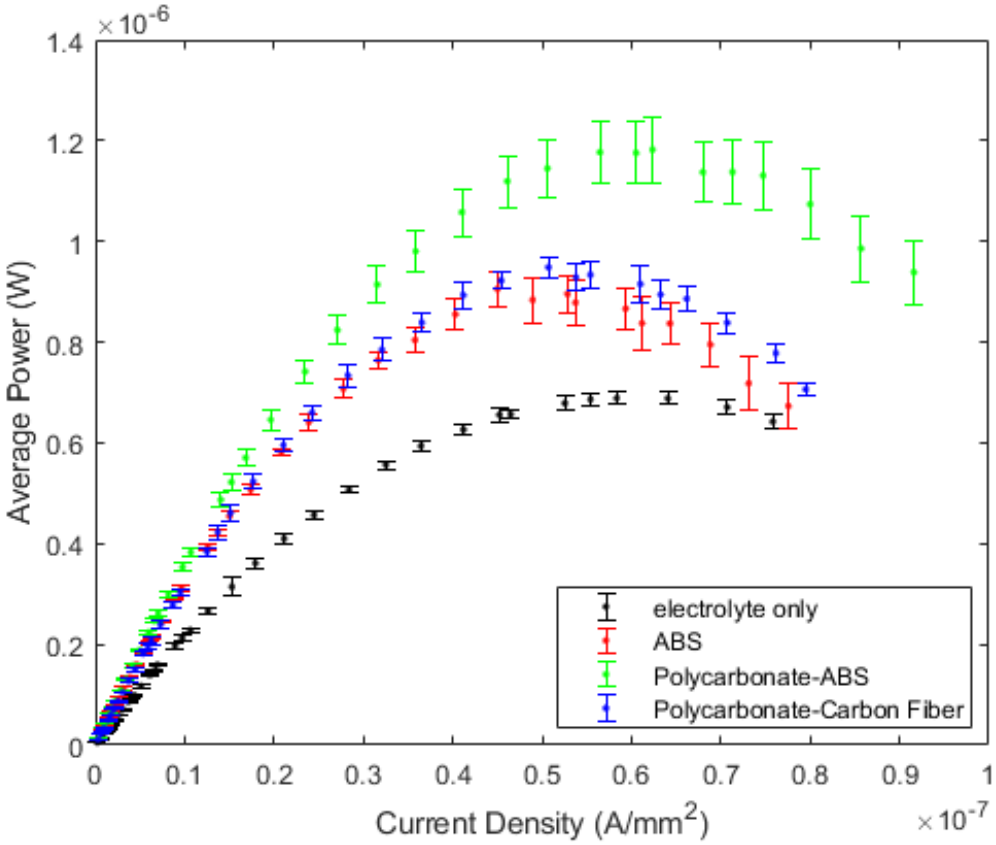

Figure 5.11: A Plot Showing The Power Output of the Thermogalvanic Bricks vs Current Density with Calculated Error Bars for the Validation Experiments.

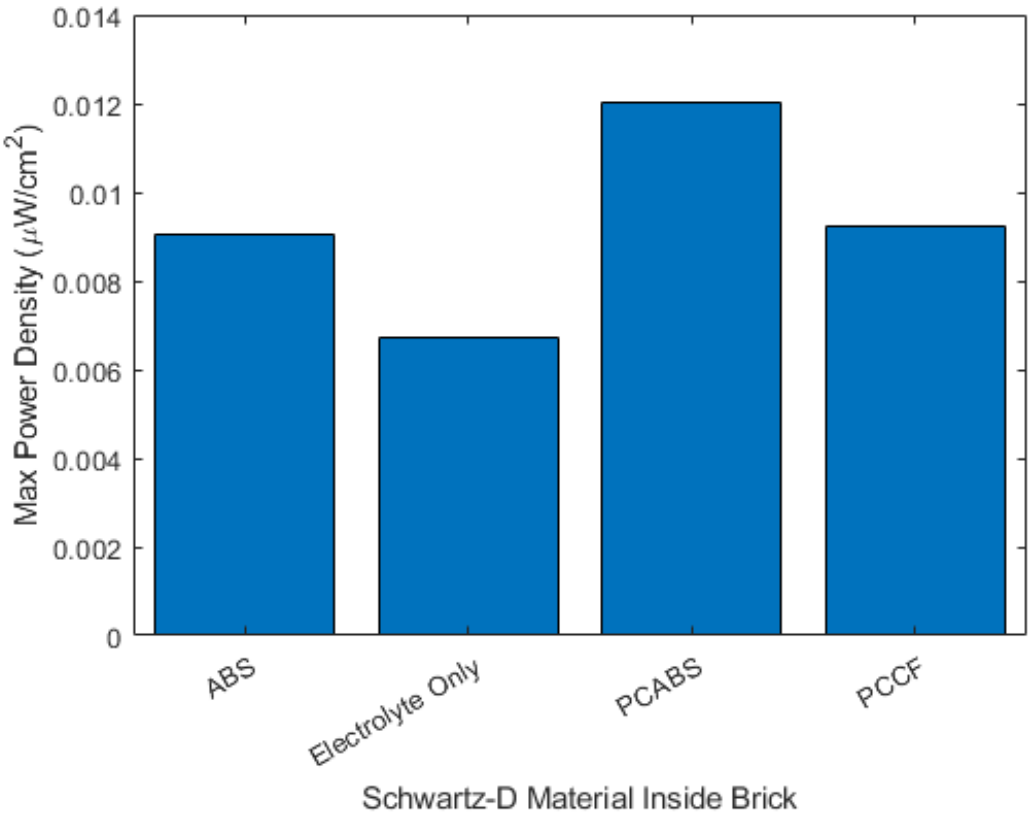

Figure 5.12: A Comparison of the Maximum Power Output for a Thermogalvanic Brick Containing Different Schwartz D Materials for the Validation Experiments.

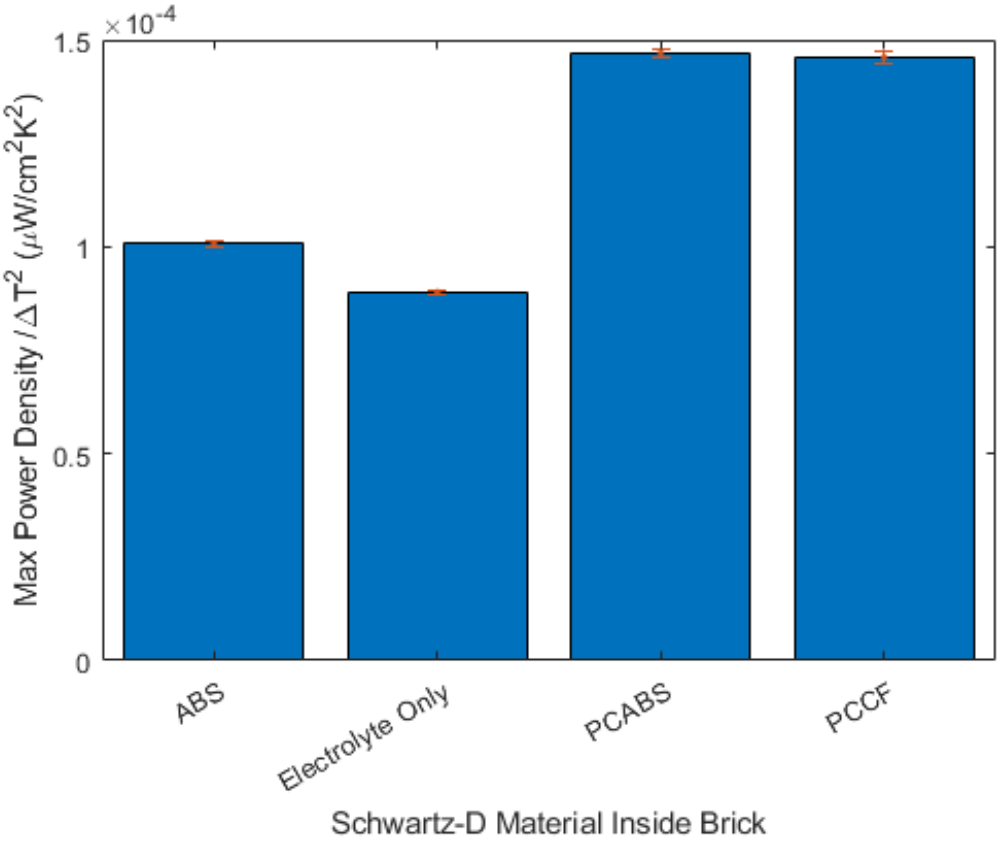

Figure 5.13: A Comparison of the Temperature Normalized Maximum Power for a Thermogalvanic Brick Containing Different Schwartz D Materials with Calculated Error Bars for the Validation Experiments.

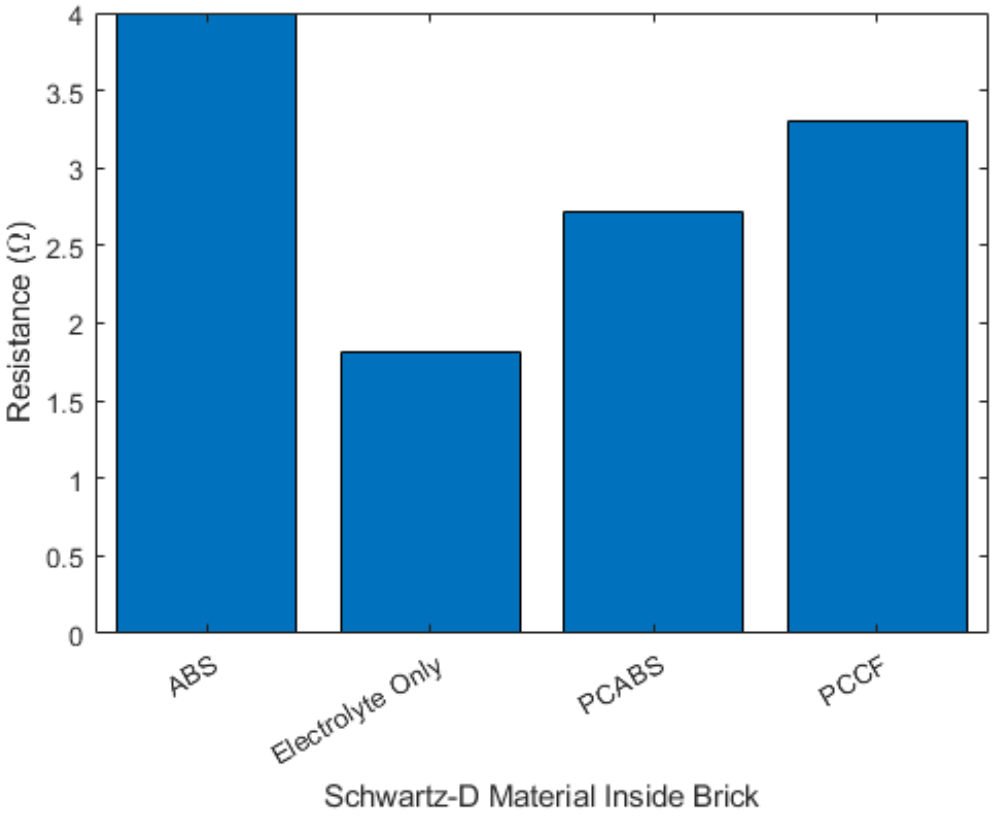

Figure 5.14: A Comparison of the Resistance Values at which the Maximum Power Density Output of the Thermogalvanic Cell were Found for a Thermogalvanic Brick Containing Different Schwartz D Materials for the Validation Experiments.

Table 5.2: Tabulated Values of Maximum Power Output and Temperature Normalized Maximum Power Output for the Validation Experiments.

	Electrolyte Only	**ABS**	**PCABS**	**PCCF**
Max Power Density Output ($\frac{\mu W}{cm^2}$)	0.00671	0.00904	0.01202	0.00923
Max Normalized Power Density Output ($\frac{\mu W}{cm^2 \cdot K^2}$)	0.8903×10^{-4}	1.0082×10^{-4}	1.4684×10^{-4}	1.4582×10^{-4}

5.2 Discussion

5.2.1 Initial Experiments

From the results of the first experiments, it can be seen that the thermal properties of the Schwartz D have an effect on the temperature difference ΔT between the copper electrodes. This is seen in Figure 5.1 where the ΔT values are plotted against time or in Figure 5.2. Interestingly, PCABS had the highest ΔT but ended up with the lowest normalized $P_{density,\Delta T}$ at $0.9981 \times 10^{-4} \frac{\mu W}{cm^2 \cdot K^2}$, as seen in Figure 5.5 and Table 5.1. On the other hand, from Figure 5.6, PCCF performed the best with a normalized power output of almost $1.5 \times 10^{-4} \frac{\mu W}{cm^2 \cdot K^2}$. These values are within the expected magnitude for the power output that is found in literature for a 0.7 M $CuSO_4$ + 0.1 M H_2SO_4 aqueous electrolyte copper thermogalvanic cell. Some of the literature values for power outputs were between $0.0087 \frac{\mu W}{cm^2}$ and $1.57 \frac{\mu W}{cm^2.}$ depending on the particular cell

configuration and electrode spacing [9, 25]. This shows the thermogalvanic brick is a promising way to harness some of the energy used for thermal regulation in a building.

Although there are large error bars, the trend for the data in Figure 5.3 can be seen to be a linear trend. This is to be expected when comparing the average cell potential and the current for a Cu/Cu^{2+} thermogalvanic cell. Because of this linear trend the formula 1.16 may be applied to find the maximum power output of the cell. Because of the error found in the cell potential data, the power output in Figure 5.4 turned out to also have a large amount of uncertainty. Even with the amount of error present in the calculated power, the trend of the data in 5.4 follows the expected parabolic shape for power versus current density in a thermoelectric or thermogalvanic cell.

Interestingly, the maximum power outputs were found at quite low resistances all under $10\,\Omega$ as seen in Figure 5.7. For both bricks containing a composite polycarbonate Schwartz D, the maximum power density output was found at an equivalent value of $3.3\,\Omega$ for the load resistance, whereas the maximum power density output for the electrolyte only was found at the lowest resistance of $1.8\,\Omega$ and ABS at the highest load resistance of $6.82\,\Omega$. This shows that the maximum power output occurs when the internal resistance of the thermogalvanic brick of this volume is quite low, as explained in Chapter 1, since $R_{int} = R_{ext}$ at the maximum power output.

5.2.2 Validation Experiments

To verify the results in the initial experiments, the tests on the thermogalvanic brick were run again with a focus on reducing the error in the measured cell potential values. Although the ΔT values were generally lower in this set of experiments (Figures 5.8 and 5.9), the normalized specific power density output values were comparable to the previous experiments; this can be seen by comparing Figures 5.13 and 5.6 and Tables 5.2 and 5.1. In both experiments the thermogalvanic brick with the

PCCF Schwartz D structure performed very well with a normalized maximum power density output of around $1.5 \times 10^{-4} \frac{\mu W}{cm^2 \cdot K^2}$. This was a 131.4% improvement compared to the baseline of electrolyte only in the first experiment and a 163.8% improvement on the electrolyte only brick in the validation experiments. In the case of PCABS, in the initial experiments it unexpectedly performed worse than the brick with only the electrolyte only, especially since it had a higher ΔT than the other bricks. In the validation experiment, PCABS performed the best of the tested thermogalvanic bricks, having a 164.9% improvement over the electrolyte only brick.

In the case of PCABS, it was seen that the power output in Figure 5.12 was actually the highest of the different materials while the maximum was obtained at a ΔT in between that of ABS and the electrolyte only bricks. The PCABS highest maximum normalized power density can be attributed to the combination of power output and ΔT value, where as for PCCF, it was found to have a max power output around that of ABS, but had the lowest ΔT in all of the tests shown here.

As for the cell potential versus current seen in Figure 5.10, similar to the data from the previous experiments, Figure 5.3, it was found to be a linear relationship. As for the power versus current density the data in 5.11 shows a smooth parabolic curve with significantly lower error in power than in Figure 5.4.

In the validation experiments, the resistance at which the maximum power is found for ABS, changed from $6.82\,\Omega$ to $4\,\Omega$ and that for PCABS changed from $3.3\,\Omega$ to $2.72\,\Omega$. On the other hand, the maximum power was found at the same resistance as the previous test for the other materials, which can be seen by comparing Figure 5.14 and 5.7. There are a couple potential reasons for this; one could be due to the amount of variation in the results of the initial experiments which caused the shift in where the max power was found. The other potential reason could be from the lower ΔT value in the validation experiment compared to the the initial experiment,

but this is less likely because the ΔT for all the validation experiments were slightly lower than in the initial experiment.

From this data, the Seebeck coefficient was calculated to compare these results with literature. The literature found the Seebeck coefficient for a 0.7 M $CuSO_4$ + 0.1 M H_2SO_4 aqueous electrolyte to be between 0.72 $\frac{mV}{K}$ and 0.84 $\frac{mV}{K}$ [9, 25]. The literature values for Seebeck coefficient were larger than what was found in this experiment as the Seebeck coefficient found here range from 0.43 $\frac{mV}{K}$ to 0.57 $\frac{mV}{K}$ as seen in Table 5.3.

Table 5.3: Tabulated Values of Seebeck Coefficient from the Experimental Data for the Thermogalvanic Brick.

	Electrolyte Only	**ABS**	**PCABS**	**PCCF**
Seebeck Coefficient ($\frac{mV}{K}$)	0.433	0.468	0.571	0.540

5.2.3 Uncertainty Analysis

To determine the repeatability and validity of the data an uncertainty analysis must be performed. The uncertainty analysis was performed on equation 1.9 to find how much the error terms affect the normalized $P_{density,\Delta T}$ [40].

$$\delta P_{density,\Delta T} = \sqrt{\left(\frac{\partial P_{density,\Delta T}}{\partial P} \cdot \delta P\right)^2 + \left(\frac{\partial P_{density,\Delta T}}{\partial \Delta T} \cdot \delta \Delta T\right)^2} \tag{5.1}$$

$$\delta P_{density,\Delta T} = \sqrt{\left(\frac{1}{\Delta T^2} \cdot \delta P_{density}\right)^2 + \left(\frac{-2P_{density}}{\Delta T^3} \cdot \delta \Delta T\right)^2} \tag{5.2}$$

From equation 5.2 it can be seen that the error is driven by the error found in the $P_{density}$ rather than that of the thermocouples. Thus, it is important to perform the

experiment in a way to try and reduce the amount of error that is found in the power density.

Table 5.4: Tabulated Values of Uncertainty for Temperature Normalized Maximum Power Output.

	Electrolyte Only	**ABS**	**PCABS**	**PCCF**
Initial Experiment Normalized Max Power Density Uncertainty ($\frac{\mu W}{cm^2 \cdot K^2}$)	$\pm 0.11322 \times 10^{-4}$	$\pm 0.10228 \times 10^{-4}$	$\pm 0.12077 \times 10^{-4}$	$\pm 0.37899 \times 10^{-4}$
Validation Experiment Normalized Max Power Density Uncertainty ($\frac{\mu W}{cm^2 \cdot K^2}$)	$\pm 0.39803 \times 10^{-6}$	$\pm 0.74122 \times 10^{-6}$	$\pm 1.0858 \times 10^{-6}$	$\pm 1.3781 \times 10^{-6}$

From the uncertainty values in Table 5.4 as well as the error bars shown in Figure 5.6 it can be seen that the error values from the initial experiment are quite large, ranging from 9% for the electrolyte only thermogalvanic brick to over 25% for the brick containing the PCCF Schwartz D structure. With such a large error of 25% on the temperature normalized max power output for PCCF, it is difficult to confirm the validity of its performance in relation to the others since the maximum values obtained for both ABS and the electrolyte only fall within the error bars of the normalized

max power density of the brick with the PCCF Schwartz D. Thus, the experiment was performed again and the error was reduced significantly for all the tests to under 1%, as seen in Figure 5.13. This was accomplished by reducing the human error in the manually recorded resistances by following a meticulous recording procedure to ensure every value of cell potential correlates correctly to a single resistance. Using these results in Figure 5.13 and Table 5.2, it can be determined that both PCCF and PCABS performed the best as the results are within the uncertainty range of each other at $1.4582 \times 10^{-4} \frac{\mu W}{cm^2 \cdot K^2}$ and $1.4684 \times 10^{-4} \frac{\mu W}{cm^2 \cdot K^2}$ respectively.

Chapter 6

RECOMMENDATIONS

There are a few recommendations that should be taken into consideration for the next iteration of the project. Firstly, because the error in normalized maximum power output is driven by the error found in the maximum power, reducing the error in the cell potential measurements—which is directly related to the power output—will greatly reduce the uncertainty found in the temperature normalized maximum power output. Next it is recommended to repeat the experiment multiple times to determine the repeatability of the results that were presented in this paper. Third, it is recommended to try and get a larger ΔT as it was found in previous literature that higher temperature differences yield higher maximum power outputs [9, 20].

Another recommendation would be to create new electrolyte taking careful consideration of the concentrations of the stock solutions used. Having a lower concentration than the 0.7 M $CuSO_4$ + 0.1 M H_2SO_4 aqueous electrolyte that was selected may have a significant impact on the magnitude of the power output.

Lastly, it is recommended to pay careful attention during the experiment to make sure the steps are followed exactly as laid out. This is especially important because the resistance values during the data collection must be input manually whenever the resistance is changed. Lack of attention to detail may cause the recording of incorrect data, which would lead to poor results.

Chapter 7

CONCLUSIONS

The current exposed electrode prototype design was able to deliver a ΔT between 7°C and 15°C. This ΔT value is significantly better than the one achieved by a full acrylic walled brick outlined in Chapter 2. Utilizing the exposed electrode design the experiment showed the promising results for PCCF 0.2 volume fraction minimal surface Schwartz D structure. The thermogalvanic brick with PCCF performed the best when comparing the temperature normalized power output to the baseline electrolyte only brick. It was found in the initial experiments that the thermogalvanic brick with a PCCF Schwartz D performed 31.4% better than that of the electrolyte only. Where as the brick with PCABS and ABS Schwartz D structures both performed slightly worse that the brick with only electrolyte at 12.5% and 0.63% respectively.

For the validation experiment it was found that the PCCF was still one of the better performers for power output with a 163.8% increase in normalized power density output compared to the electrolyte only brick. The best performance was actually found to be PCABS, which performed the worst in the initial experiments. The thermogalvanic brick with PCABS performed with a 164.9% increase in normalized power density output compared with the electrolyte only. The PCABS thermogalvanic brick performed at the highest normalized power output as a result of a combination of the high power output while maintaining a ΔT between the ABS and the electrolyte only bricks. This largest power output can be attributed a the thermal attributes of PCABS and the flow of Cu^{2+} ions through the gaps of the PCABS Schwartz D. This is known because physically, a thermogalvanic cell would want to contain a high thermal resistance to maintain a high ΔT, while also allowing promoting the movement

of ions through the electrolyte.

The outputs of the thermogalvanic brick may seem small on the magnitude of micro watts, but one must remember there will be more than a single brick in a building. As calculated prior in Chapter 1, it was found that on average for a single story, one family home, over $8,700$ bricks are required for only the outer walls. This would yield maximum power outputs of the whole single story house at a minimum of $0.0138\,W$ for the electrolyte only brick house and a maximum of over $0.02\,W$ for Cu/Cu^{2+} thermogalvanic bricks containing a PCCF or PCABS Schwartz D lattice.

These results from the initial experiments can only be taken after careful consideration because the uncertainty found in the temperature normalized max power density reach up to 25% of the calculated maximum for PCCF. With the uncertainty value at 25% for the PCCF thermogalvanic brick, the normalized maximum power density for ABS and the electrolyte only bricks are within the error of PCCF. This means, even though PCCF was found to have the highest maximum power density, the next experiment that is performed, the power output of the thermogalvanic brick with a PCCF Schwartz D may perform worse than that of ABS or only the electrolyte.

From the validation experiments, which have uncertainty values under 1% for the normalized maximum power density, the PCCF Schwartz D thermogalvanic brick was verified having a high normalized power output very close to what was found in the initial experiments, but PCABS was also found to have a similar normalized max power density within the margin of error of that of PCCF. This means both the PCCF Schwartz D and PCABS Schwartz D perform equivalently better than a Cu/Cu^{2+} thermogalvanic brick without Schwartz D.

This improvement in the performance of the bricks containing the Schwartz D compared to one without may be attributed to the actual 3D printed materials. One thing to consider when dealing with fused deposition modeling (FDM) 3D printers,

like the Zortrax M200 used in this project, is that every printed object will be unique. Even for the same 3D model, a model printed from the same 3D printer may end up with slight changes in geometry or surface roughness because of how FDM printing works. This slight change in geometries between the different Schwartz D structures may have created a pathway for the copper(II) ions and electrons to travel through in the PCABS version.

Chapter 8

FUTURE WORK

There are a few areas of consideration that would be helpful to understand the internal workings of the thermogalvanic brick. One would be the evaluation of natural convection of the aqueous electrolyte in the brick to better understand how the thermal interactions within the brick occur. Understanding these thermal interactions may allow for the selection of a better material to use for the Schwartz D structure. Along the lines of thermal analysis, a thermal analysis of the brick including the Schwartz D structure will need to be performed to see how adding a minimal surface scaffold will change the thermal properties in the brick. This thermal analysis may help explain the temperature differences found in the experimental results of this thesis.

One major consideration for future work would be to revise the experimental measurement setup to utilize a four point measurement technique. By using the four point method, the cell potential measurements should be much more accurate, as the four point method uses a second set of probes for the measurement. Using a second set of probes, a negligible current will flow across the second set of probes which allows for only the voltage drop across the thermogalvanic brick to be captured.

Along the lines of the Schwartz D minimal surface structures, it will be good to explore various other volume fractions of Schwartz D aside from the 0.2 volume fraction that was tested in these experiments. Exploration of some novel materials for the Schwartz D that are both thermally insulative and electrically conductive may help promote higher power outputs from the thermogalvanic brick allowing for higher a ΔT.

Another key area of interest would be the actual electrolyte used in the brick. It may not be very good to have a liquid electrolyte present in the final production brick, as it may be more prone to leaks as compared to a gelled or solid electrolyte. Some potential electrolyte options would be a ferricyanide/ferrocyanide, a ferrocene/-ferrocenium, a iodide/tri-iodide, or even a cobalt based electrolyte.

The final consideration for future work would be changing the acrylic casing material to see how that would change the power output of the thermogalvanic brick. One idea would be to get much thinner walls since the load bearing part of the brick is supposed to be the Schwartz D structure. This would allow for a larger active electrode area as well as more electrolyte and a larger electrode spacing. These are all factors that have been found to change the power output of a thermogalvanic cell.

REFERENCES

[1] BP, "BP statistical review of world energy 2018," *BP Energy Outlook*, vol. 67, June 2018.

[2] P. Denholm, Y.-H. Wan, M. Hummon, and M. Mehos, "An analysis of concentrating solar power with thermal energy storage in a california 33scenario," *National Renewable Energy Laboratory (NREL)*, mar 2013.

[3] S. Sadat, L. Haling, P. Phelan, and R. Wang, "Materials for high temperature thermal storage in buildings." A Part of the Micro Urban Solar Integrated Concentrators (MUSIC) Project, Arizona State University, 2014.

[4] I. E. A. (IEA), "Renewables 2018: Analysis and forecasts to 2023," *Market Report Series*, 2018.

[5] G. B. Moment, *A Translation of Luigi Galvani's "De Viribus Electricitatis in Motu Musculari Commentarius" -Commentary on the Effect of Electricity on Muscular Motion. Robert Montraville Green Luigi Galvani: Commentary on the Effects of Electricity on Muscular Motion. Margaret Glover Foley.* 30 Hillside Avenue, Cambridge, Massachusetts: Elizabeth Licht, 1953.

[6] W. B. Jensen, *Classic Voltaic Cells*, vol. 8. Cincinnati, Ohio: Oesper Collections University of Cincinnati, 2015.

[7] J. T. Stock, M. V. Orna, *et al.*, *Electrochemistry, past and present*, vol. 390. ACS Publications, 1989.

[8] A. J. Debethune, T. S. Licht, and N. Swendeman, "The temperature coefficients of electrode potentials," *Journal of The Electrochemical Society*, vol. 106, no. 7, 1959.

[9] A. Gunawan, *Electrolyte- and Transport-Enhanced Thermogalvanic Energy Conversion.* PhD dissertation, Arizona State University, 2015.

[10] E. Woolley, Y. Luo, and A. Simeone, "Industrial waste heat recovery: A systematic approach," *Sustainable Energy Technologies and Assessments*, vol. 29, pp. 50 – 59, 2018.

[11] H. Jouhara and A. G. Olabi, "Editorial: Industrial waste heat recovery," *Energy*, vol. 160, pp. 1 – 2, 2018.

[12] H. Jouhara, N. Khordehgah, S. Almahmoud, B. Delpech, A. Chauhan, and S. A. Tassou, "Waste heat recovery technologies and applications," *Thermal Science and Engineering Progress*, vol. 6, pp. 268 – 289, 2018.

[13] I. Abd Rahim, M. Z. Mohd Zain, and N. Z. Asmuin, "Study on energy converter from waste heat of automobile engine," *Applied Mechanics and Materials*, vol. 663, pp. 317–321, 2014.

[14] K. Smith, *Feasibility of thermoelectrics for waste heat recovery in conventional vehicles*. NREL/TP ; 540-44247, Golden, CO: National Renewable Energy Laboratory, 2009.

[15] C. G. Hoehne, "Quantifying vehicle waste heat: A case study of phoenix, arizona," *Center for Earth Systems Engineering and Management (CESEM), Arizona State University (ASU)*, 2018.

[16] I. E. A. (IEA), *Transition to Sustainable Buildings*. France: International Energy Agency, 2013.

[17] J. Z. Woodruff, P. Brenner, A. P. Buccellato, and D. B. Go, "Environmentally opportunistic computing: A distributed waste heat reutilization approach to energy-efficient buildings and data centers," *Energy and Buildings*, vol. 69, pp. 41 – 50, 2014.

[18] A. Burlacu, G. Sosoi, R. Ștefan Vizitiu, M. Bărbuță, C. D. Lăzărescu, V. Ciocan, and A. A. Șerbănoiu, "Energy efficient heat pipe heat exchanger for waste heat recovery in buildings," *Procedia Manufacturing*, vol. 22, pp. 714 – 721, 2018. 11th International Conference Interdisciplinarity in Engineering, INTER-ENG 2017, 5-6 October 2017, Tirgu Mures, Romania.

[19] I. Dincer, "On thermal energy storage systems and applications in buildings," *Energy and Buildings*, vol. 34, no. 4, pp. 377 – 388, 2002.

[20] T. I. Quickenden and Y. Mua, "A review of power generation in aqueous thermogalvanic cells," *Journal of The Electrochemical Society - J ELECTROCHEM SOC*, vol. 142, pp. 3985–3994, 11 1995.

[21] T. Quickenden and C. Vernon, "Thermogalvanic conversion of heat to electricity," *Solar Energy*, vol. 36, no. 1, pp. 63 – 72, 1986.

[22] N. J. Agar, "Thermogalvanic cells," *Advances in Electrochemistry and Electrochemical Engineering*, pp. 31–121, 1963.

[23] D. Al-Masri, M. Dupont, R. Yunis, D. R. MacFarlane, and J. M. Pringle, "The electrochemistry and performance of cobalt-based redox couples for thermoelectrochemical cells," *Electrochimica Acta*, vol. 269, pp. 714 – 723, 2018.

[24] A. Gunawan, H. Li, C.-H. Lin, D. A. Buttry, V. Mujica, R. A. Taylor, R. S. Prasher, and P. E. Phelan, "The amplifying effect of natural convection on power generation of thermogalvanic cells," *International Journal of Heat and Mass Transfer*, vol. 78, pp. 423 – 434, 2014.

[25] A. Gunawan, C. Lin, D. Buttry, V. Mujica, R. Taylor, R. Prasher, and P. Phelan, "Liquid thermoelectrics: Review of recent and limited new data of thermogalvanic cell experiments," *Microscale Thermophysical Engineering*, vol. 17, pp. 304–323, 11 2013.

[26] S. W. Lee, Y. Yang, H.-W. Lee, H. Ghasemi, D. Kraemer, G. Chen, and Y. Cui, "An electrochemical system for efficiently harvesting low-grade heat energy," *Nature Communications*, vol. 5, pp. 3942 EP –, May 2014. Article.

[27] H. Li, A. Gunawan, P. E. Phelan, D. A. Buttry, V. Mujica, R. A. Taylor, and R. S. Prasher, "Electrode separation and operating orientation: Mechanisms for maximizing performance of Cu/Cu^{2+} aqueous thermogalvanic cells," *ASME 2013 International Mechanical Engineering Congress and Exposition*, vol. 6, no. 56284, p. V06AT07A074, 2013.

[28] C.-H. Lin, A. Gunawan, P. E. Phelan, D. A. Buttry, V. Mujica, R. A. Taylor, and R. Prasher, "Optimization of cell configuration for maximizing performance of a Cu/Cu^{2+} aqueous thermogalvanic cell," *ASME International Mechanical Engineering Congress and Exposition*, vol. 6, no. 45226, pp. 541–547, 2012.

[29] G. Qian, Y. Lu, Y. Huang, Z. Li, X. Yu, and A. P. Roskilly, "Simulation study of ferricyanide/ferrocyanide concentric annulus thermocell with different electrode spacing and cell direction," *Energy Procedia*, vol. 142, pp. 374 – 380, 2017. Proceedings of the 9th International Conference on Applied Energy.

[30] J. L. Sheean, "The beginnings of electrochemical activities," *Journal of Chemical Education*, vol. 7, no. 1, p. 33, 1930.

[31] J. Wu, J. J. Black, and L. Aldous, "Thermoelectrochemistry using conventional and novel gelled electrolytes in heat-to-current thermocells," *Electrochimica Acta*, vol. 225, pp. 482 – 492, 2017.

[32] L. Yang, H. Sun, S. Wang, L. Jiang, and G. Sun, "A solid state thermogalvanic cell harvesting low-grade thermal energy," *International Journal of Hydrogen Energy*, vol. 42, no. 41, pp. 25877 – 25881, 2017.

[33] I. Kolb, Edward J., "The thermogalvanic process," *ProQuest Dissertations and Theses*, p. 101, 1982. Copyright - Database copyright ProQuest LLC; ProQuest does not claim copyright in the individual underlying works; Last updated - 2016-05-03.

[34] Dimensions, "Overview: Publication metrics related to thermogalvanic cells." *Digital Science & Research Solutions, Inc.*, https://app.dimensions.ai, accessed 2018-10-1, 2018.

[35] G. Rosengarten, "Micro urban solar integrated concentrators (MUSIC)." U.S. – Australia Solar Energy Collaboration (USASEC), September 2012.

[36] U. S. C. Bureau, "Characteristics of new housing." *United States Department of Housing and Urban Development*, https://www.census.gov/construction/chars/completed.html, accessed 2018-10-1, 2017.

[37] D. C. Harris, *Quantitative Chemical Analysis*, vol. 7. New York: W. H. Freeman and Company, 2007.

[38] Y. Yan and J. A. Malen, "Periodic heating amplifies the efficiency of thermoelectric energy conversion," *Energy Environ. Sci.*, vol. 6, pp. 1267–1273, 2013.

[39] D. A. Kaminski and M. K. Jensen, *Introduction to Themal and Fluids Engineering*. John Wiley & Sons, Inc., 2005.

[40] FDA, USDS, and NIST, "Multi-agency radiological laboratory analytical protocols manual," *MARLAP: Planning, Assessment, Implementation*, vol. 3, 2004.

APPENDIX A

EXTRA DATA

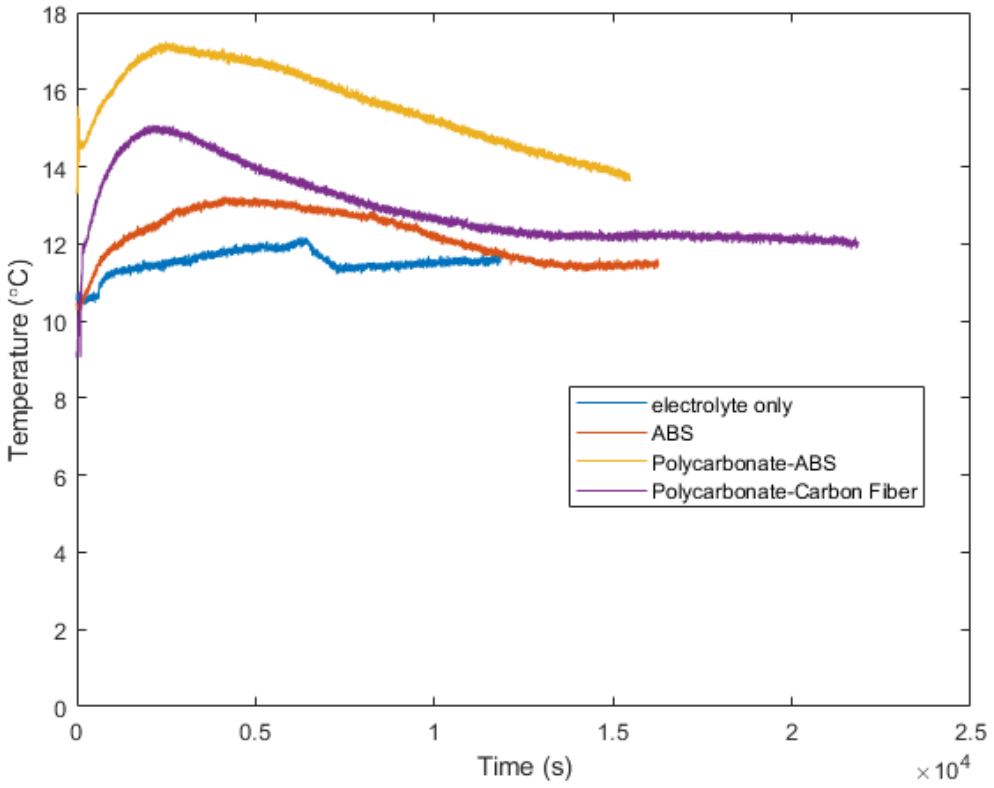

Figure A.1: Plot of Change in Temperature vs Time for the Experiments on the Thermogalvanic Brick for the Initial Experiments.

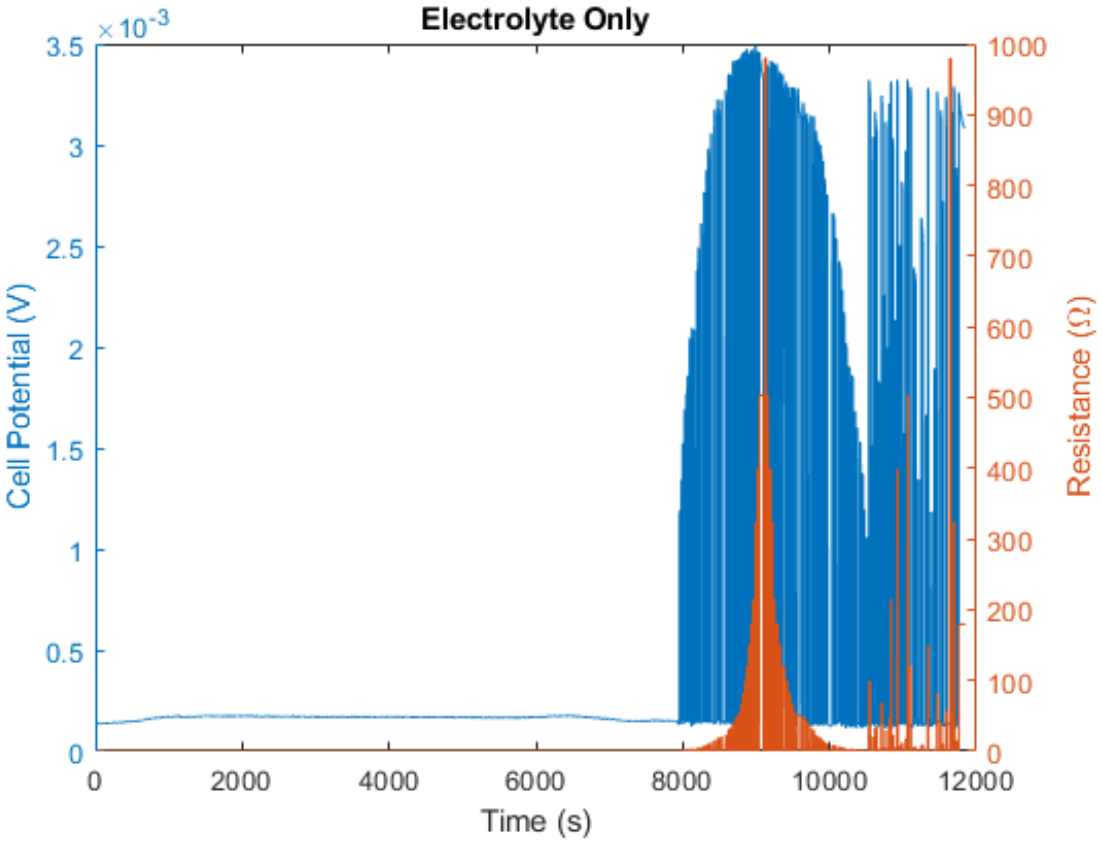

Figure A.2: Cell Potential and Resistance Plotted Against Time for the Thermogalvanic Brick Without A Schwartz D Structure for the Initial Experiments.

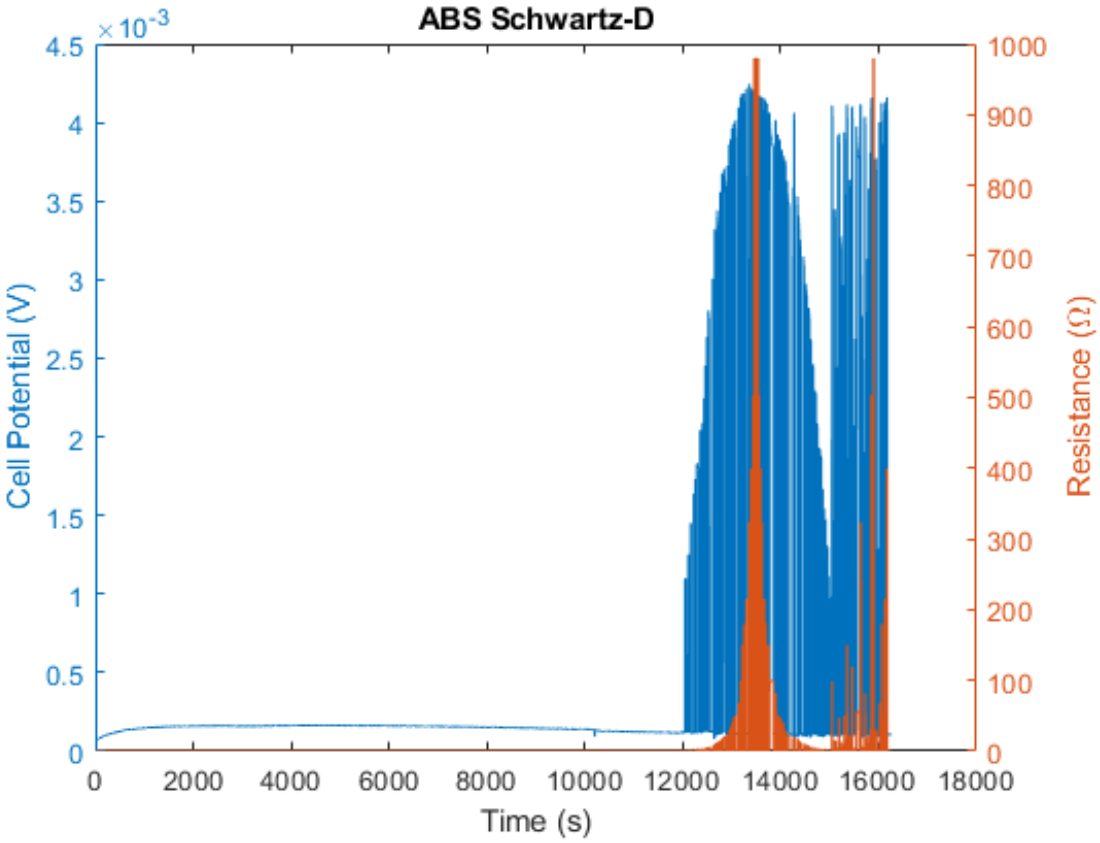

Figure A.3: Cell Potential and Resistance Plotted Against Time for the Thermogalvanic Brick Using an ABS Schwartz D Structure for the Initial Experiments.

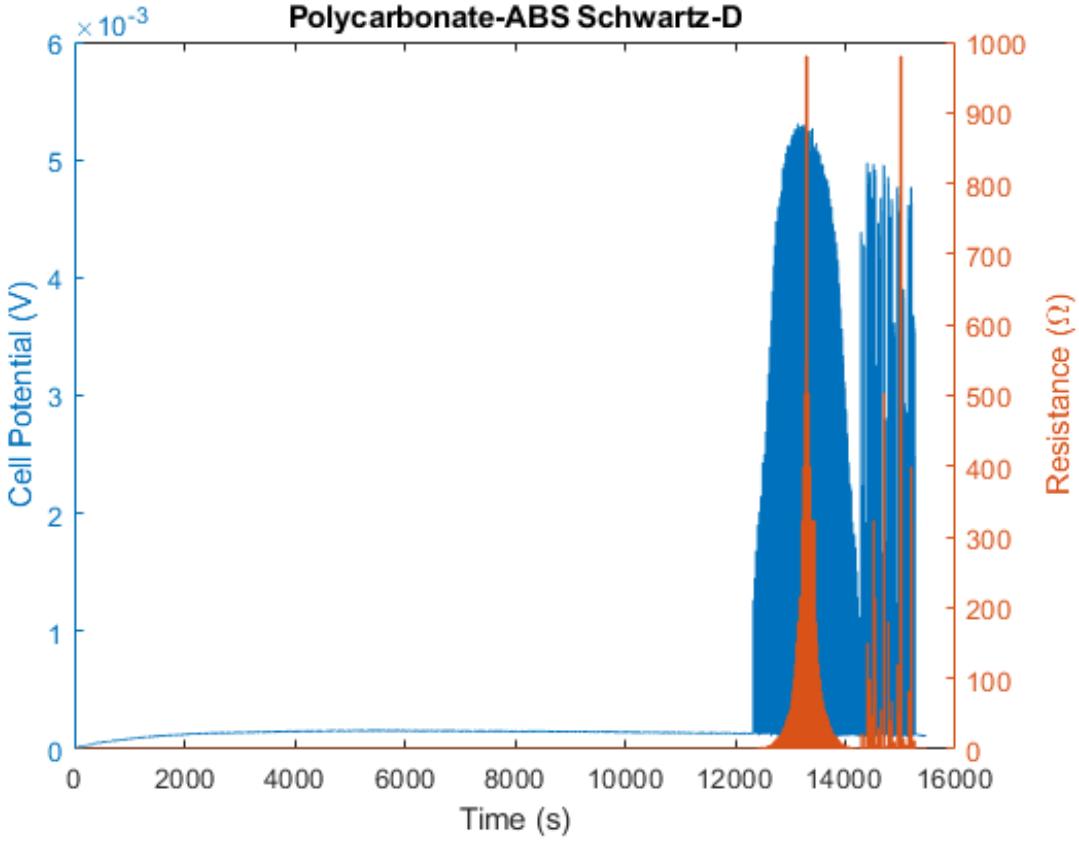

Figure A.4: Cell Potential and Resistance Plotted Against Time for the Thermogalvanic Brick Using an PCABS Schwartz D Structure for the Initial Experiments.

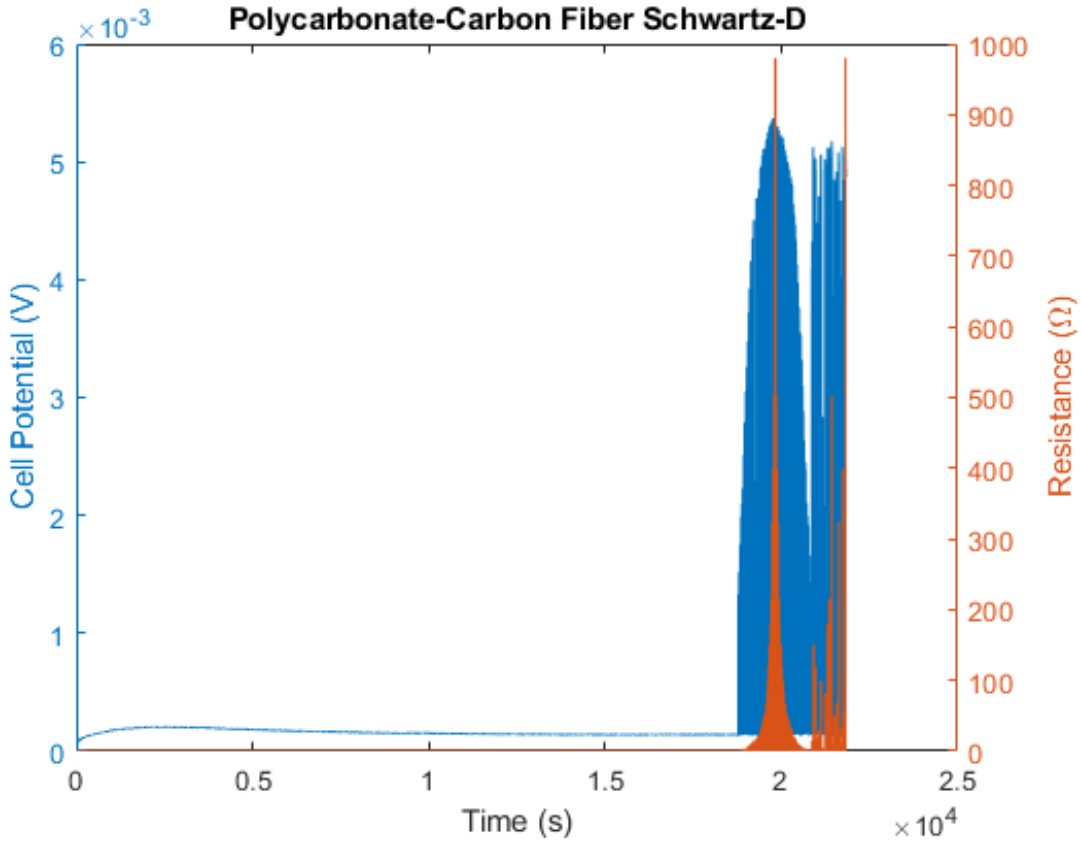

Figure A.5: Cell Potential and Resistance Plotted Against Time for the Thermogalvanic Brick Using an PCCF Schwartz D Structure for the Initial Experiments.

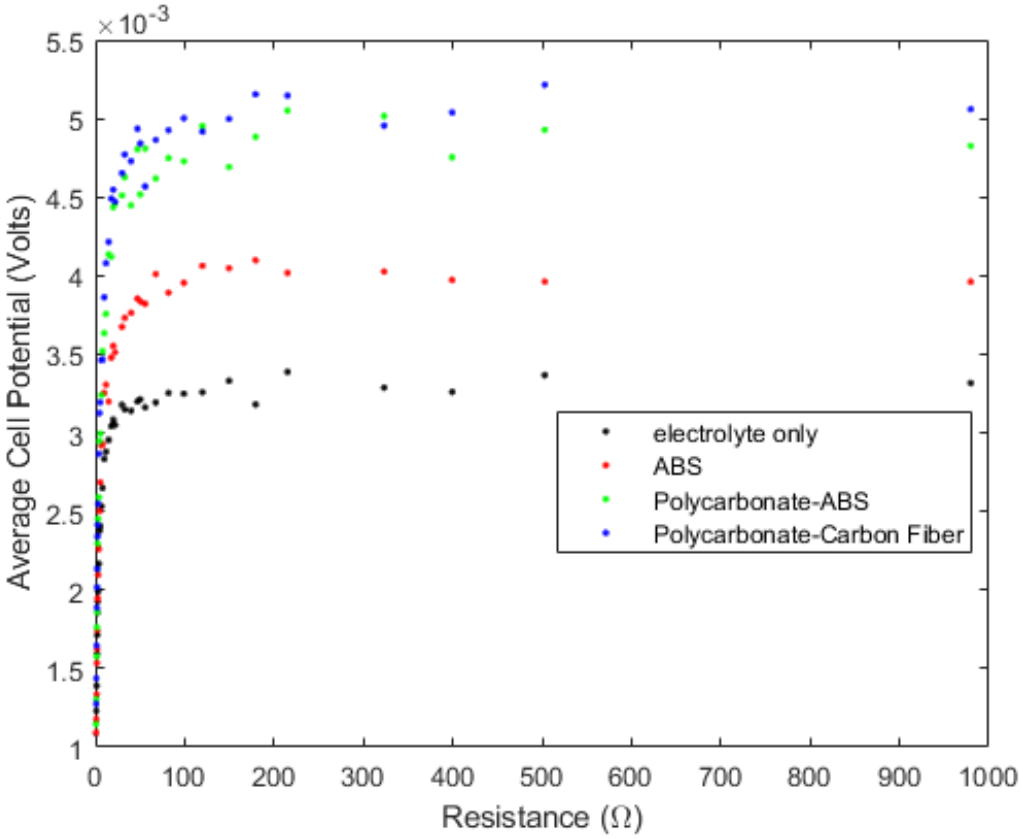

Figure A.6: A Plot Showing Average Cell Potential Vs Resistance for the Initial Experiments.

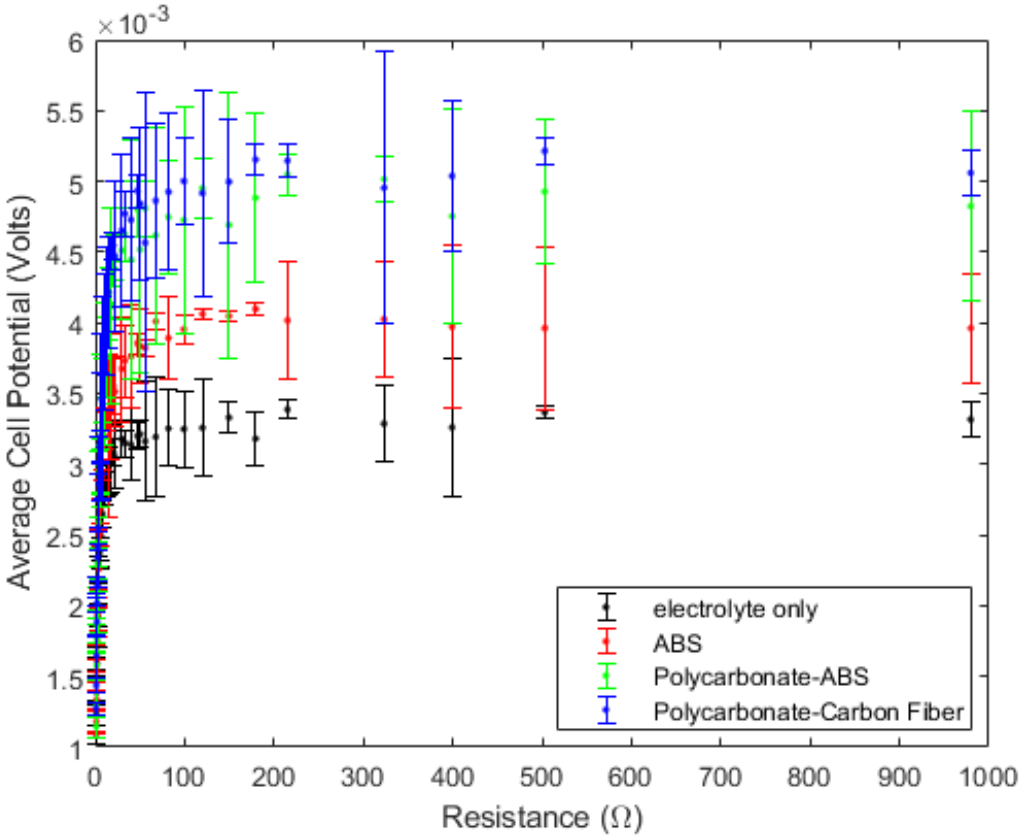

Figure A.7: A Plot Showing Average Cell Potential Vs Resistance with Calculated Error Bars for the Initial Experiments.

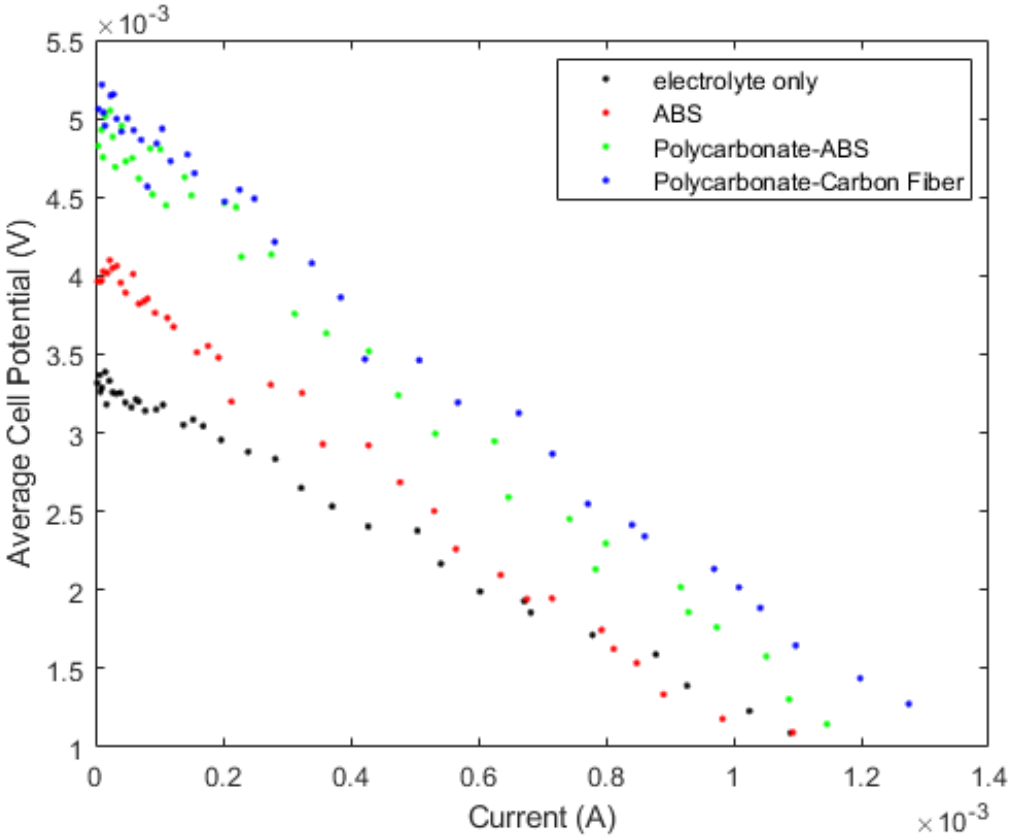

Figure A.8: A Plot Showing Average Cell Potential Vs Current for the Initial Experiments.

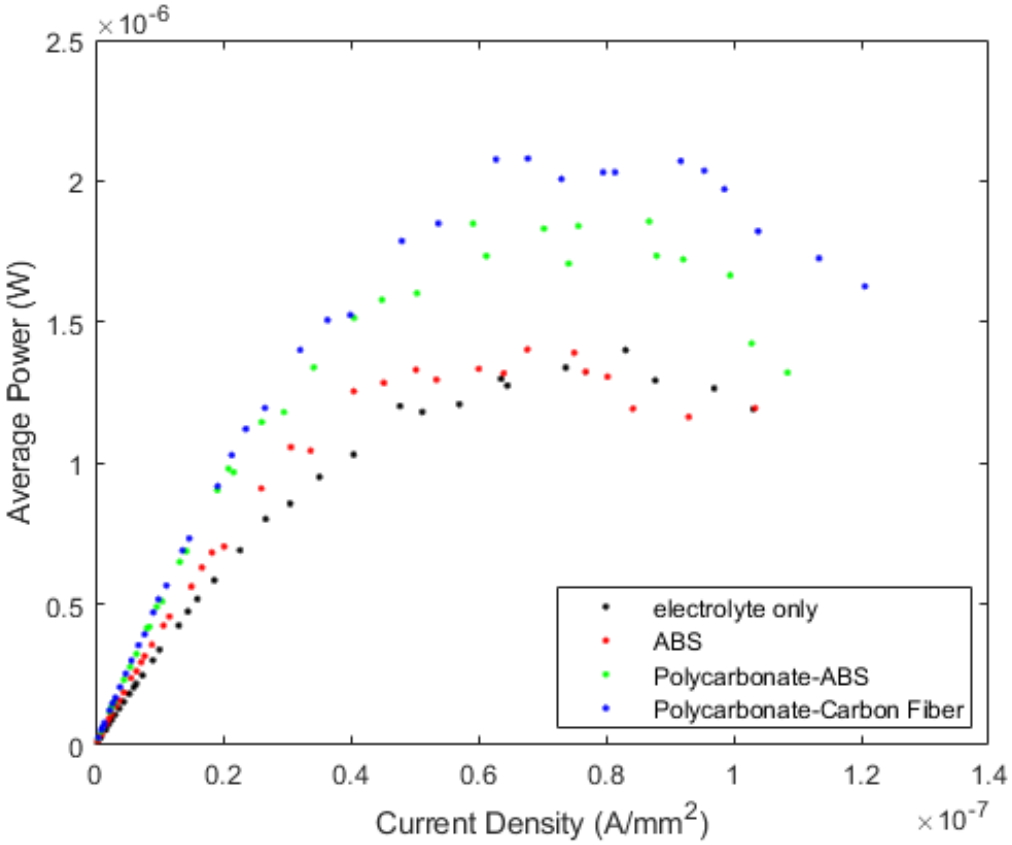

Figure A.9: A Plot Showing The Power Output of the Thermogalvanic Bricks vs Current Density with Calculated Error Bars for the Initial Experiments.

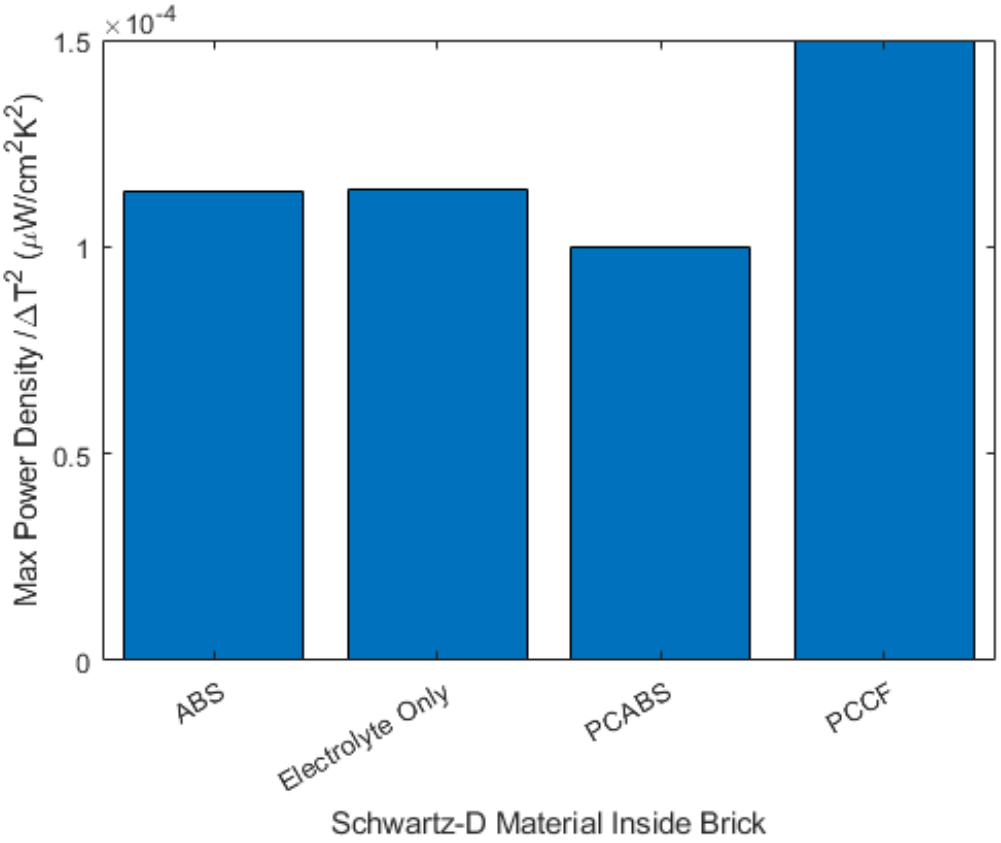

Figure A.10: A Comparison of the Temperature Normalized Maximum Power for a Thermogalvanic Brick Containing Different Schwartz D Materials for the Initial Experiments.

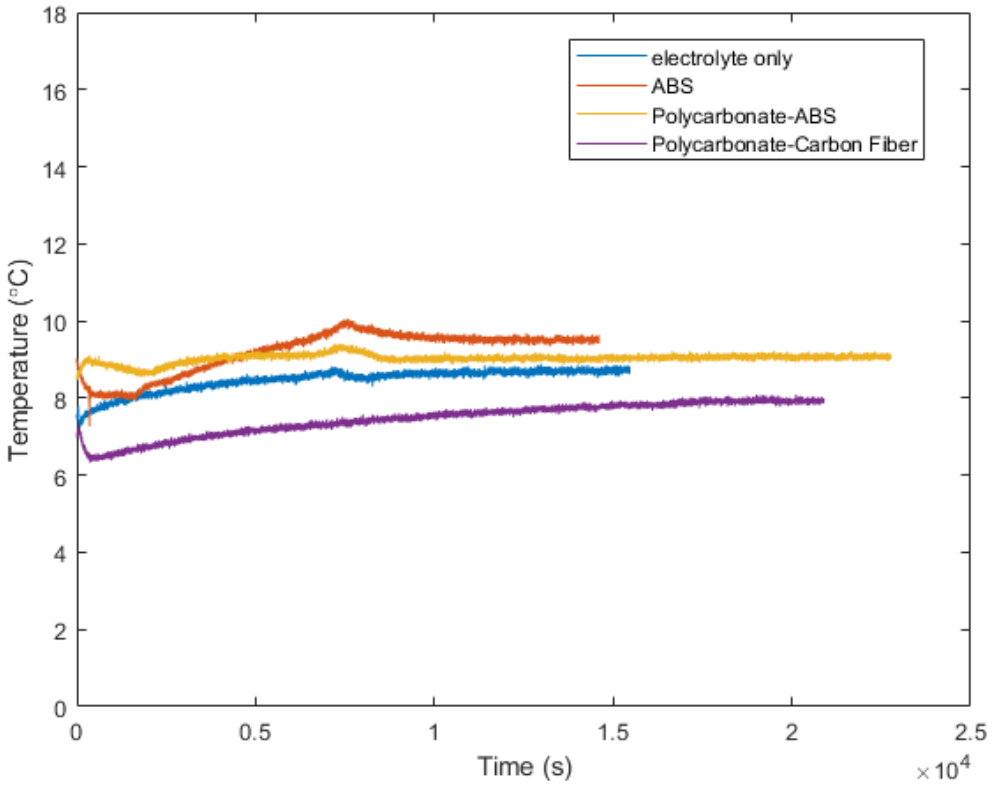

Figure A.11: Plot of Change in Temperature vs Time for the Experiments on the Thermogalvanic Brick for the Validation Experiments.

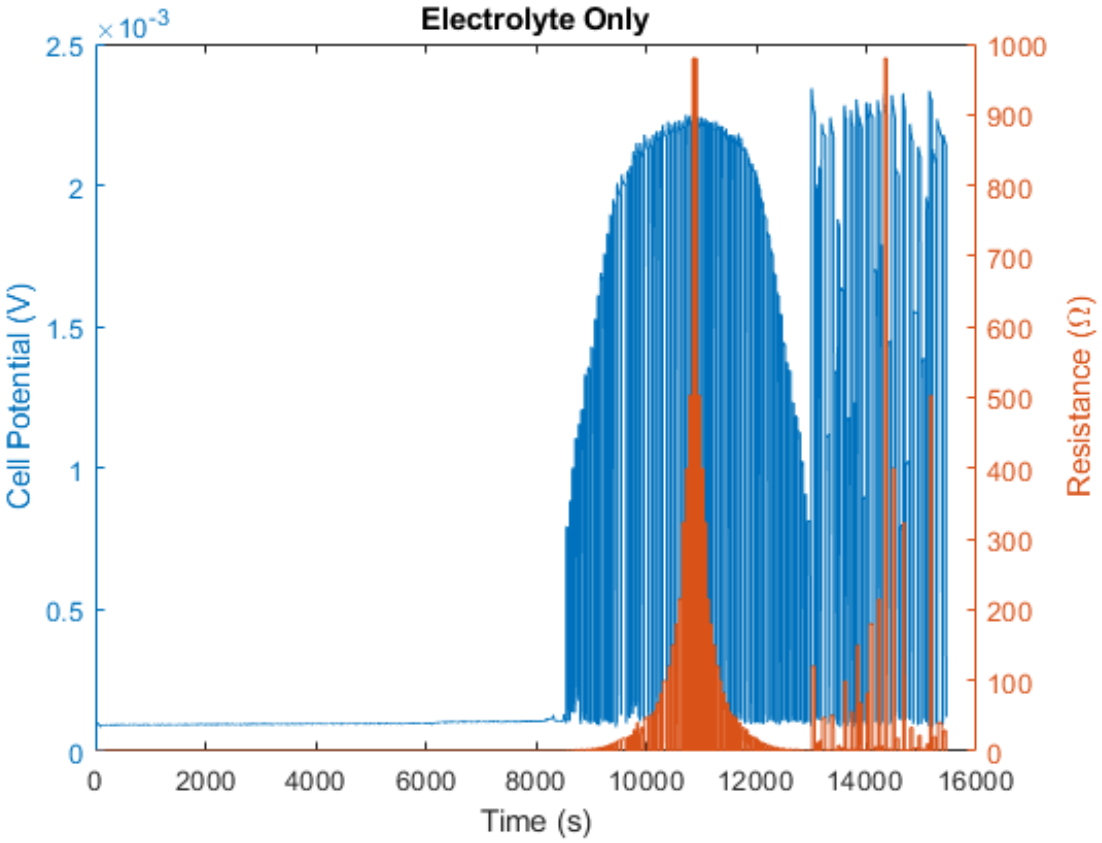

Figure A.12: Cell Potential and Resistance Plotted Against Time for the Thermogalvanic Brick Without A Schwartz D Structure for the Validation Experiments.

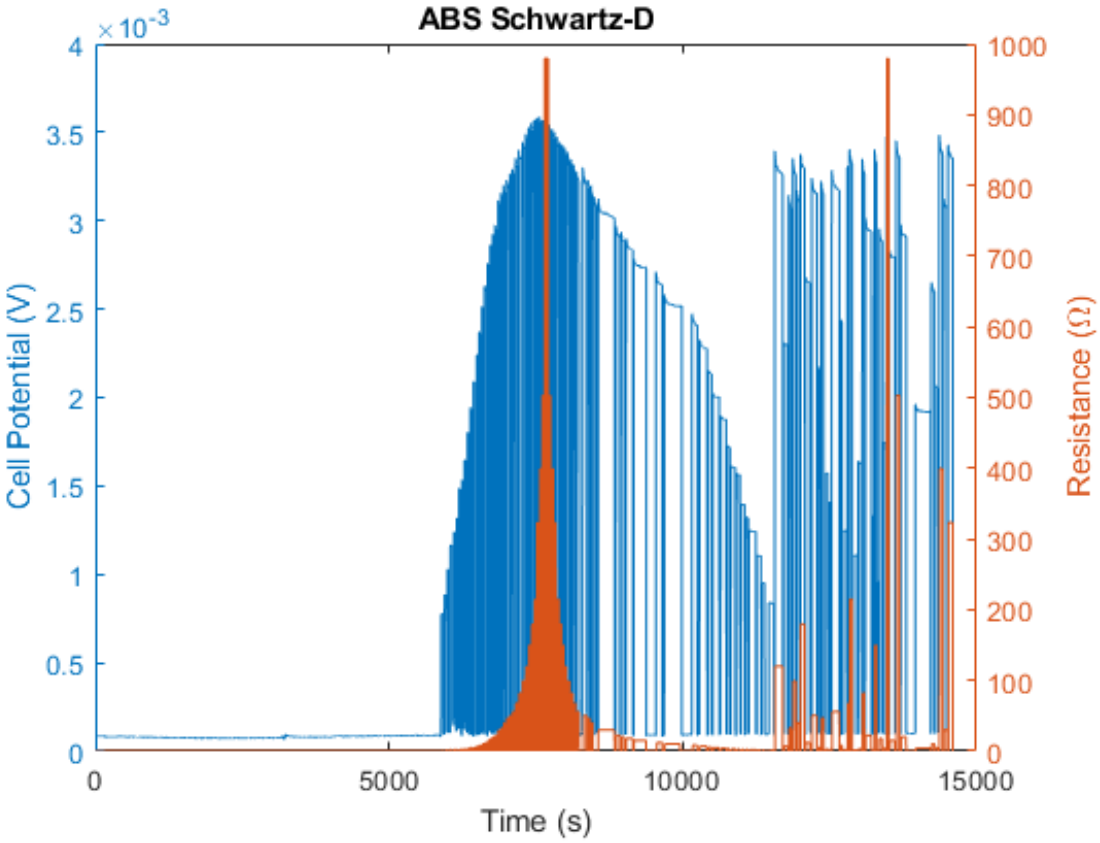

Figure A.13: Cell Potential and Resistance Plotted Against Time for the Thermogalvanic Brick Using an ABS Schwartz D Structure for the Validation Experiments.

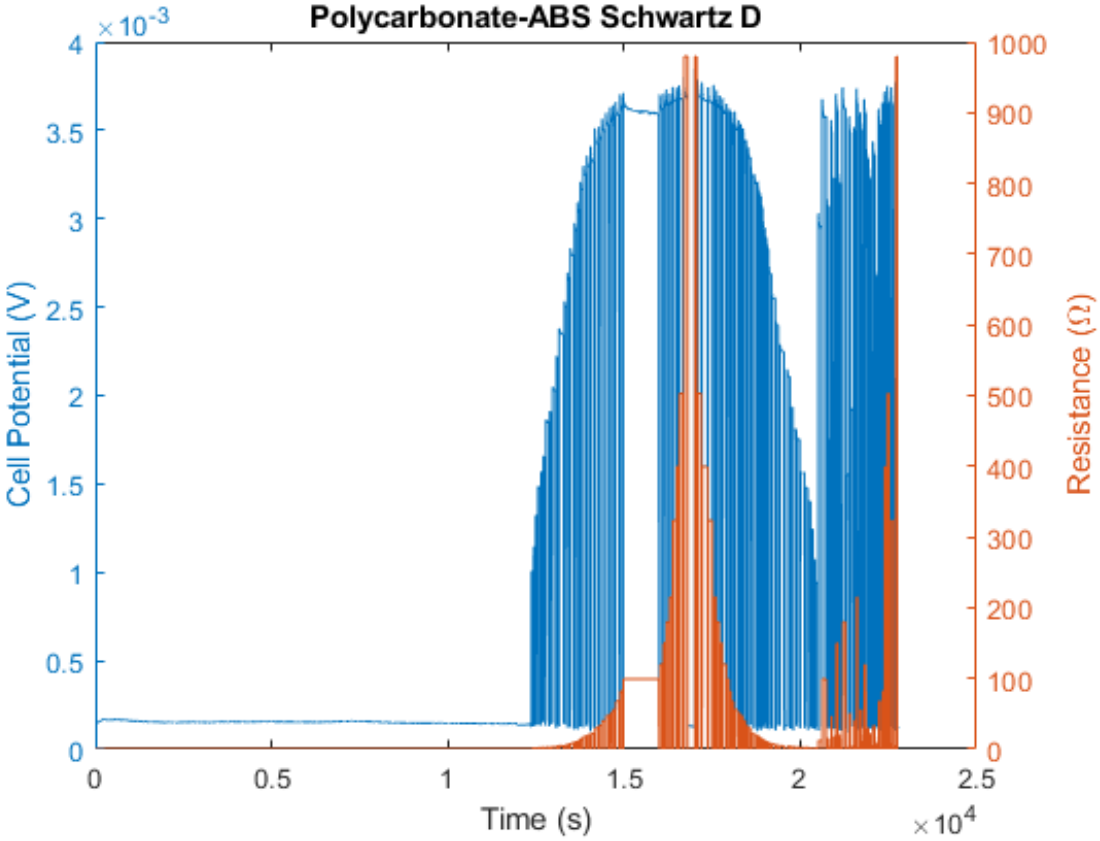

Figure A.14: Cell Potential and Resistance Plotted Against Time for the Thermogalvanic Brick Using an PCABS Schwartz D Structure for the Validation Experiments.

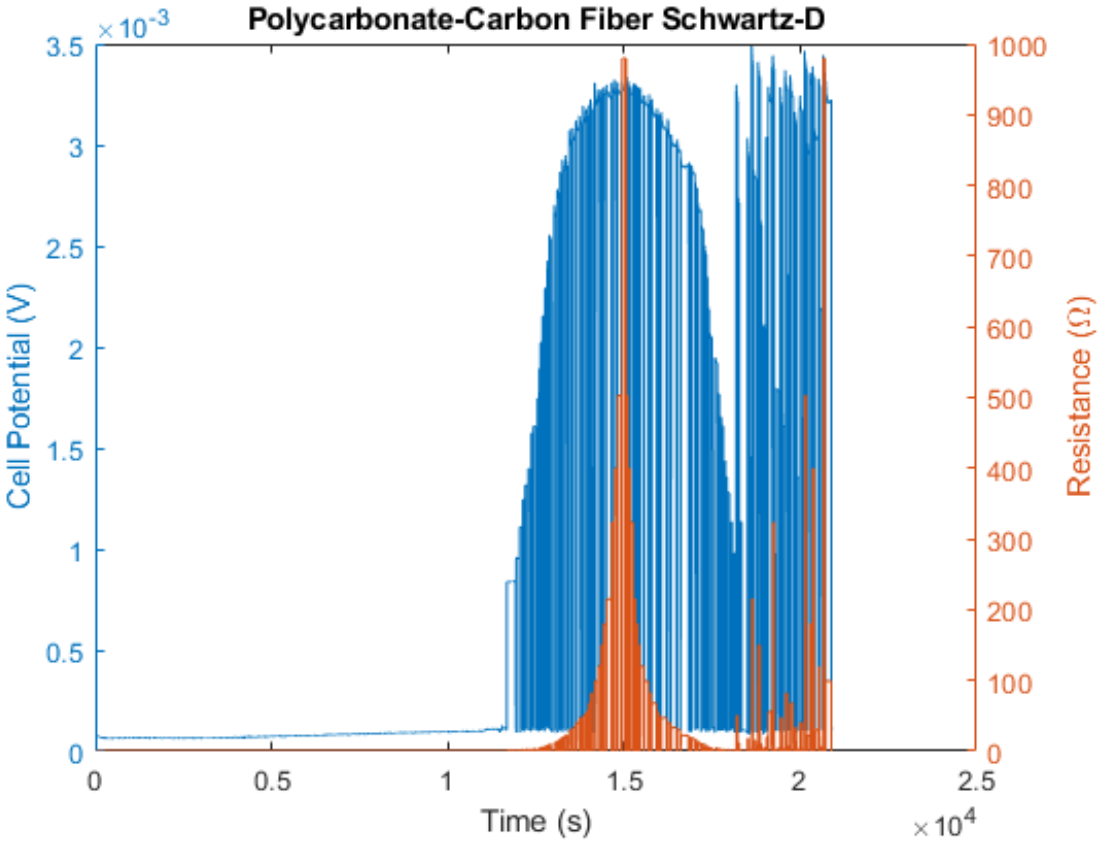

Figure A.15: Cell Potential and Resistance Plotted Against Time for the Thermogalvanic Brick Using an PCCF Schwartz D Structure for the Validation Experiments.

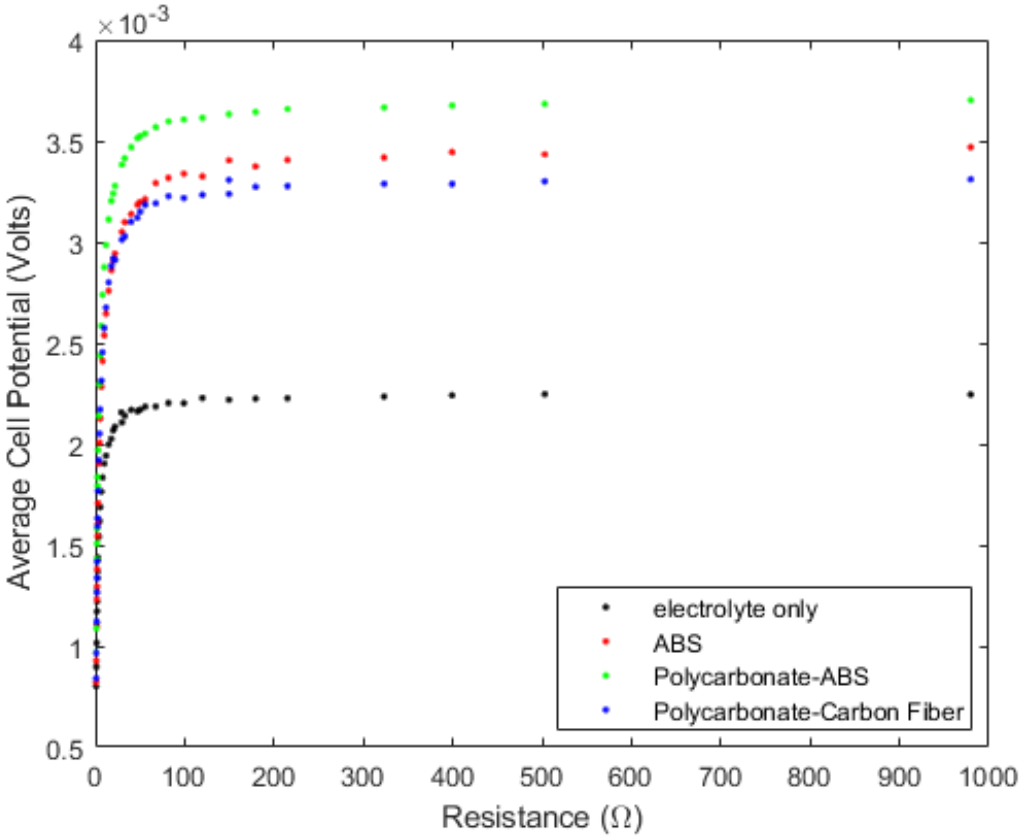

Figure A.16: A Plot Showing Average Cell Potential Vs Resistance for the Validation Experiments.

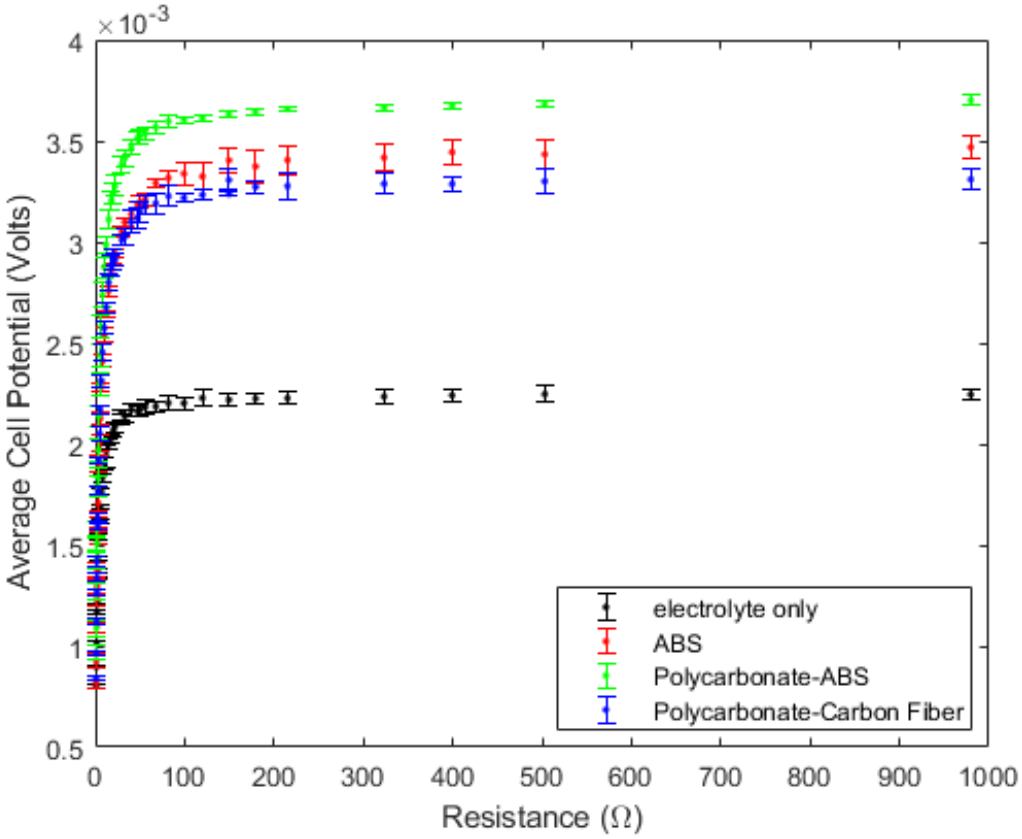

Figure A.17: A Plot Showing Average Cell Potential Vs Resistance with Calculated Error Bars for the Validation Experiments.

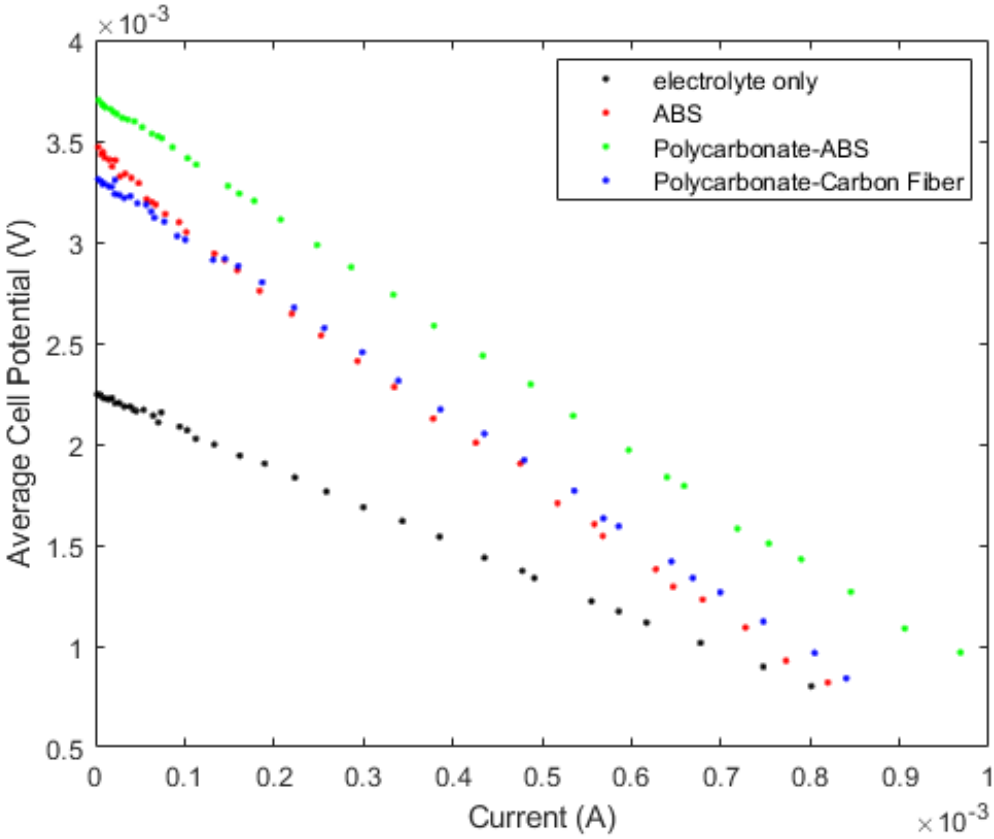

Figure A.18: A Plot Showing Average Cell Potential Vs Current for the Validation Experiments.

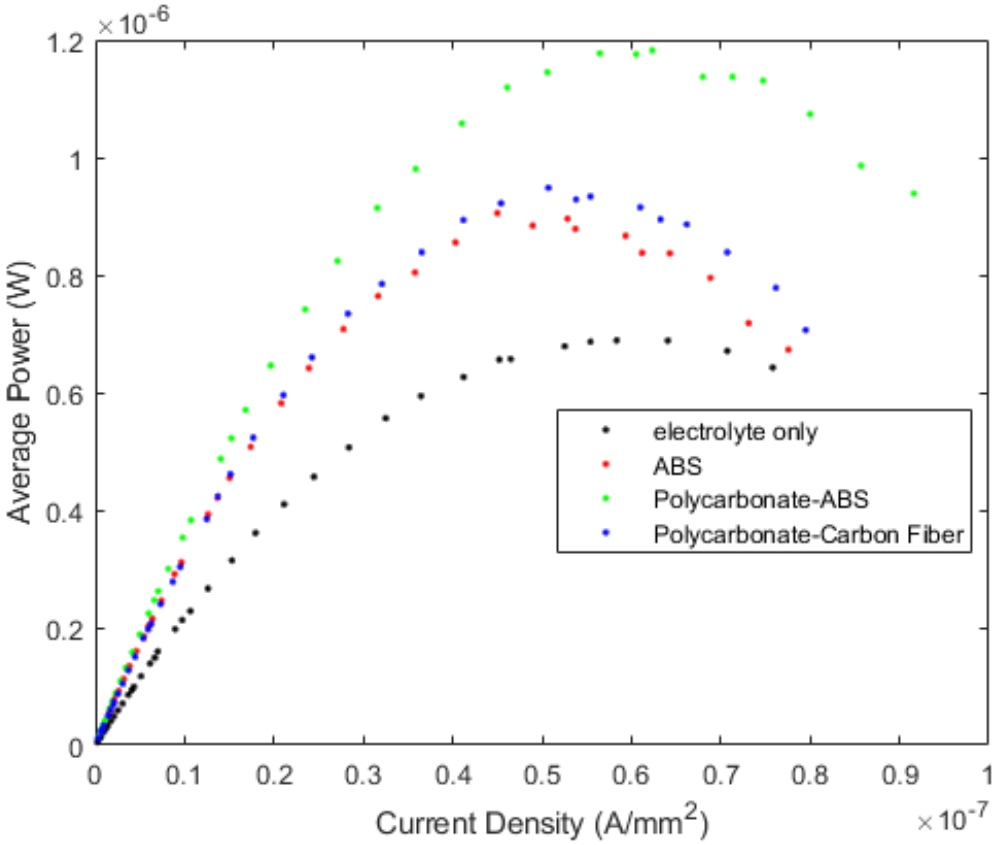

Figure A.19: A Plot Showing The Power Output of the Thermogalvanic Bricks vs Current Density with Calculated Error Bars for the Validation Experiments.

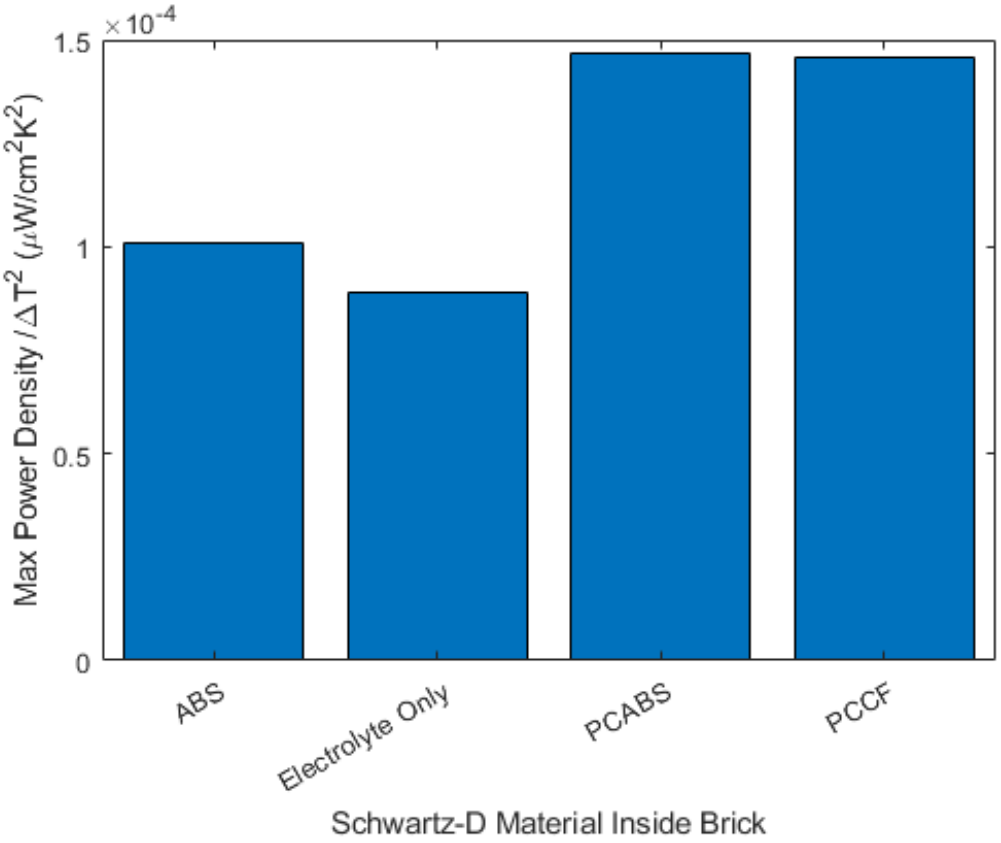

Figure A.20: A Comparison of the Temperature Normalized Maximum Power for a Thermogalvanic Brick Containing Different Schwartz D Materials for the Validation Experiments.